Title: Independent genomic trajectories shape adaptation to life on land across animal lineages

Authors: Gemma I. Martínez-Redondo[1,2] †*, Klara Eleftheriadi[1]†*, Judit Salces-Ortiz[1], Nuria Escudero[1], Fernando Ángel Fernández-Álvarez[3,4], Belén Carbonetto[1], Carlos Vargas-Chávez[1], Raquel García-Vernet[1,2], Javier Palma-Guerrero[1,5], Libe Rentería[1], Iñaki Rojo[6], Cristina Chiva[7,8], Eduard Sabidó[7,8], Aureliano Bombarely[9] & Rosa Fernández[1]*

Affiliations:

[1] Metazoa Phylogenomics and Genome Evolution Lab, Institute of Evolutionary Biology (CSIC-UPF), Barcelona (Spain)

[2] Universitat de Barcelona, Barcelona (Spain)

[3] Centro Oceanográfico de Gijón, Instituto Español de Oceanografía, Gijón (Spain)

[4] Institut de Ciències del Mar (ICM-CSIC), Barcelona (Spain)

[5] Current address: Research Institute of Organic Agriculture (FiBL), Aargau (Switzerland)

[6] Citizen scientist, Sopelana (Spain)

[7] Centre for Genomic Regulation (CRG), Barcelona Institute of Science and Technology (BIST), Barcelona (Spain)

[8] Universitat Pompeu Fabra (UPF), Barcelona (Spain)

[9] Instituto de Biología Molecular y Celular de Plantas, Valencia (Spain)

†These authors contributed equally to this work, order was chosen by dice rolling.

* Corresponding authors: gemma.martinez@ibe.upf-csic.es, klara.eleftheriadi@ibe.upf-csic.es, rosa.fernandez@ibe.upf-csic.es

Abstract: How animals repeatedly adapted to life on land is a central question in evolutionary biology. While terrestrialisation occurred independently across animal phyla, it remains unclear whether shared genomic mechanisms underlie these transitions. We combined large-scale comparative genomics, machine learning, and multi-omics data—including proteomics and transcriptomics from stress experiments in 17 species—to investigate the genomic basis of terrestrial adaptation. Gene co-expression networks revealed that stress-response hubs were largely lineage-specific, yet converged in function through the co-option of ancient gene families. Phylogenomic and machine learning analyses supported a dominant role for early-evolving genes, enriched in stress-related functions, with extensive gene loss at terrestrialisation nodes. Our findings support a model of functional convergence via lineage-specific repurposing of conserved genomic elements.

Main Text:

The transition of animals to land —terrestrialisation—is one of the most transformative events in the evolutionary history. Coming from relatively stable marine environments, animals underwent radical physiological and morphological adaptations to cope with the environmental challenges of life on land, including desiccation, higher oxygen concentration, ultraviolet radiation, and changes in osmotic pressure and chemical exposure[1–5]. As such, terrestrialisation represents not just a change in habitat, but a major functional reconfiguration of animal biology. Fossil evidence suggests the first land exploration by marine arthropod relatives occurred around 470 million years ago[4–6], likely driven by the need to mate or lay eggs out of predators' reach. Over millions of years, terrestrial habitats became progressively inhabited as environments became more hospitable due to the biota's own influence[1,7,8]. Unlike plants, which terrestrialised only once[9], animals (Metazoa) have independently transitioned to land multiple times across at least nine out of the 31 animal phyla (Fig. 1a,b). Terrestrialisation in animals is highly heterogeneous—many species remain semi-terrestrial, requiring water at specific life stages, while only a few complete their entire life cycles on land[10,11]. These transitions occurred via direct marine-to-terrestrial routes or freshwater intermediaries utilised by certain groups like platyhelminthes, molluscs, crabs, and vertebrates[12–16] (Fig. 1c). This rich tapestry of terrestrialisation, characterised by diverse dependencies on water, varied environmental routes to land, and staggered timelines, underscores the multifaceted nature of this evolutionary achievement.

Most previous studies have focused on individual species[17,18], specific phyla[19–22] or particular gene families[23,24], without assessing whether genomic adaptation to terrestrial life involved convergent genomic changes across all animal phyla, or arose through lineage-specific mechanisms.. To address this, we conducted a broad comparative analysis of nearly 1,000 animal species, integrating genome-wide data with expression profiles from stress experiments, along with proteomic data, in diverse aquatic and terrestrial invertebrates. We also used machine learning to identify gene families associated with habitat type. By tracing the evolutionary origins and functions of these genes, we provide a comprehensive view of how animals have genomically adapted to life on land through repeated, but distinct, evolutionary routes.

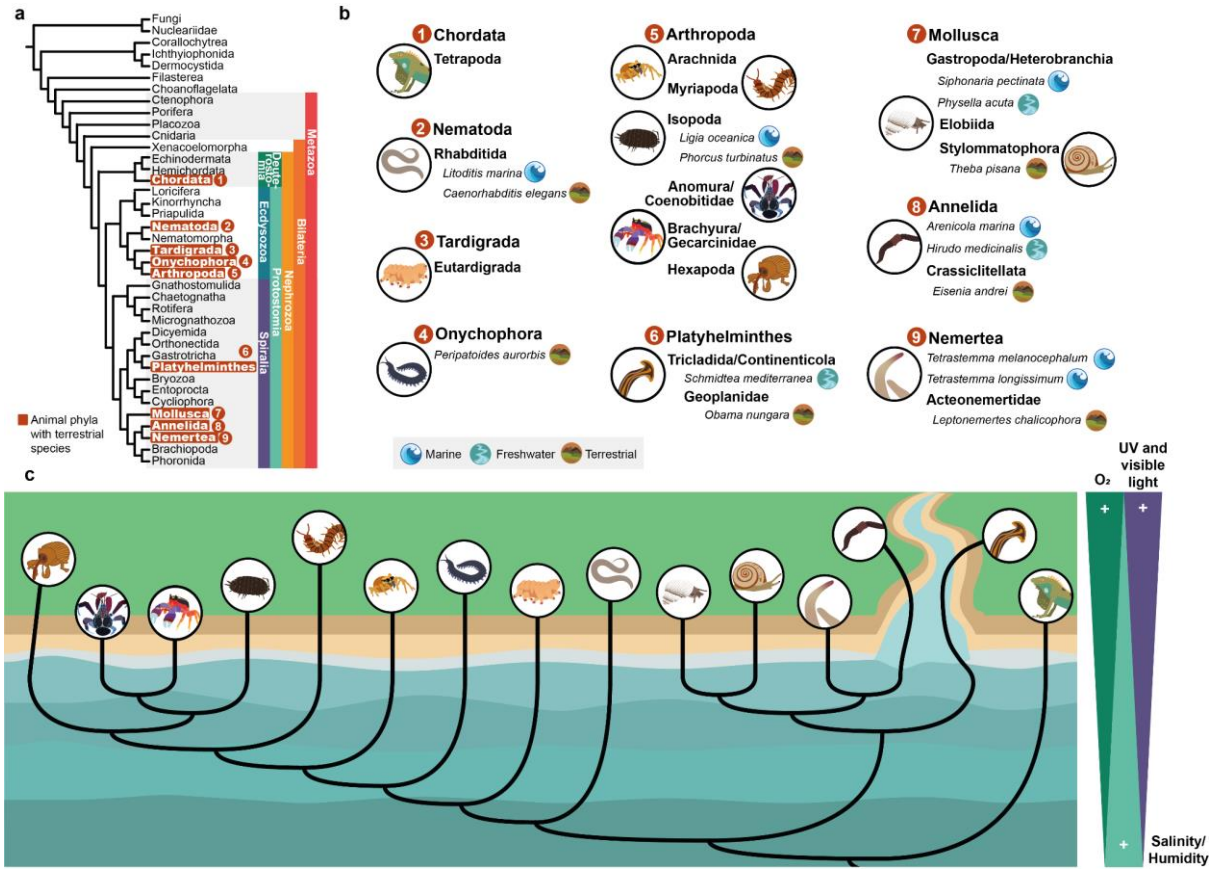

Figure 1. Animal terrestrialisation at a glance. a, Animal tree of life highlighting the phyla where there has been at least one terrestrialisation event. **b**, Main animal terrestrialisation events discussed in this work, with the species used in the "re-terrestrialisation" stress experiments. **c**, Simplified view of paths towards terrestrial life in animals, and the differences in some abiotic factors between habitats. *[High resolution figure can be accessed here: https://drive.google.com/file/d/1dkqUuouQuJlIScnSeQYCrV1LbU81hQx3/view?usp=sharing]*.

A kingdom-wide reconstruction of animal gene repertoire evolution

To understand the evolutionary foundations of animal terrestrialisation, we first reconstructed the origin and diversification of gene families across the animal kingdom. We performed orthology inference on high-quality protein-coding gene sets from 973 species (960 animals, Table S1), spanning all 31 recognised animal phyla, resulting in over 500,000 orthogroups (which we use as a proxy for gene families and vice versa). Using phylogenomic reconciliation, we dated the evolutionary origin of each gene family and quantified the patterns of gene gain and loss across the metazoan tree (Fig. 2a). Our results showed that most gene families originated early in animal evolution, with many orthogroups established during the initial diversification of Metazoa, as previously proposed[25–27]. Notably, and contrary to previous research, we identified a striking burst of gene innovation at the base of Protostomia (the lineage that includes all invertebrates that later transitioned to terrestrial environments), probably unveiled by our higher taxonomic sampling. This finding highlights a key but previously underrecognised phase of genomic innovation in early protostome evolution (Fig. 2b). In contrast, gene losses were much lower at deeper nodes, followed by independent bursts of losses, which are gradually reduced towards the tips of the tree, congruent with previous findings[25–27], and consistent with a biphasic model of evolution[28].

Our extensive dataset allowed us to study 15 independent animal terrestrialisation events represented by two or more species, encompassing both ancient transitions deep in the metazoan tree and more recent, lineage-specific events closer to the tips of the phylogeny (Fig. 1b). Relatively few gene families originated at the nodes corresponding to the predicted emergence of terrestrial lineages. Instead, these nodes were marked by extensive gene loss, in some cases exceeding gene gains by more than an order of magnitude (Fig. 2c, Table S2). This pattern was held consistently across independent terrestrialisation events in and within different phyla. We then performed a GO enrichment analysis to identify the functions of gained and lost gene families (Fig. S1-90). Both gained and lost gene families were enriched in functions associated with response to stimuli (such as UV radiation or oxygen), DNA repair and maintenance, reproduction and meiosis, cell division and cell cycle regulation, reproduction, immunity and defense mechanisms, sensory perception and signaling, transport and homeostasis, and developmental processes related to organ formation (e.g., fin development GO term was enriched in lost gene families in tetrapods, Fig. S88) and environmental adaptation. Moreover,

GO terms showed moderate functional convergence (measured as semantic similarity between the GO terms; see Methods) between independent terrestrial lineages (Fig. S91a,b). For instance, when we compared hexapods and tetrapods, we found GO terms enriched in functions related to skin protection: cuticle development for hexapods (Fig. S1) and keratinization for tetrapods (Fig. S85). This suggests a mechanism of paired gain and loss of genes with overlapping functions, reshaping the gene repertoire during terrestrialisation. The predominance of gene loss over gain at key phylogenetic nodes indicates that, during the transition to land, gene repertoire evolution may have relied more on the removal of functionally redundant or environmentally dispensable genes, facilitated by mutational robustness, rather than relying primarily on de novo gene innovation.

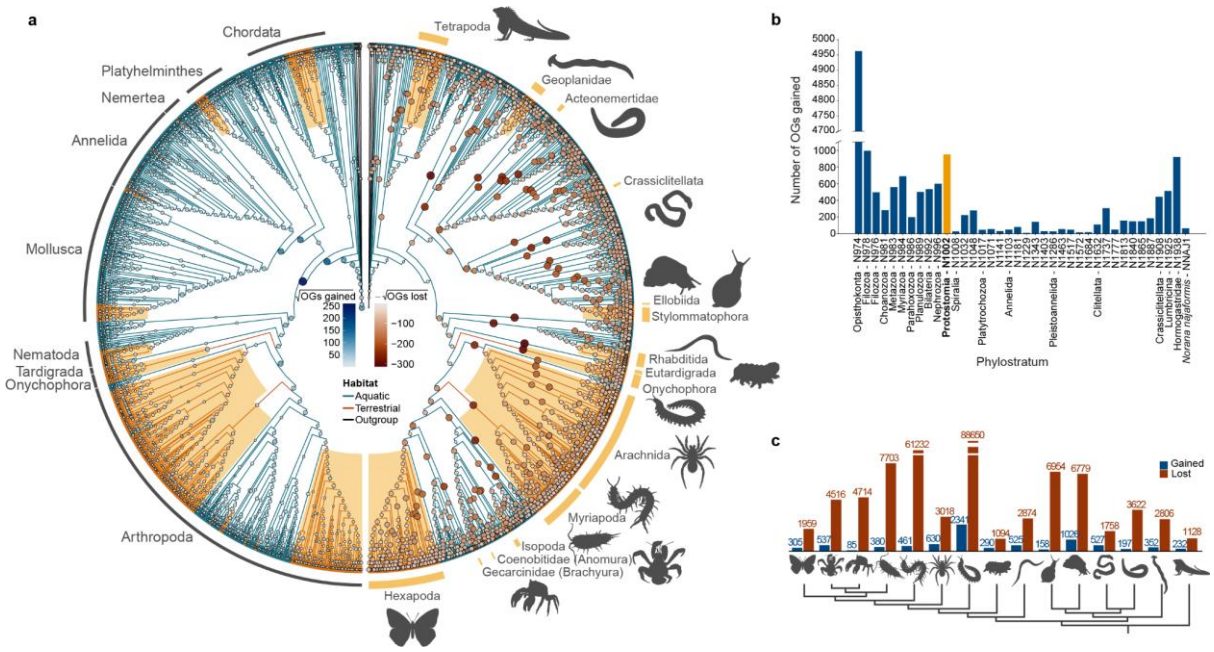

Figure 2. Gene family evolution across the animal kingdom. a, Mirror phylogeny of 960 animal species plus outgroups showing the number of gene families gained (left, blue) and lost (right, brown) at each internal branch. Terrestrial lineages are highlighted in yellow; the right phylogeny labels individual terrestrial lineages, while the left phylogeny indicates the phyla containing those lineages. **b**, Phylostratigraphic origin of all genes in all nodes in a representative species (the earthworm *Norana najaformis,* Annelida), highlighting the gene gain burst in Protostomia (in yellow). **c**, Comparison of gene gain and loss across the 15 terrestrial clades with independent terrestrialisation events. *[High resolution figure can be accessed here: https://drive.google.com/file/d/1NlSumu6-77SZtOMdFJu_xf9CUrTB5PoH/view?usp=sharing]*.

Lack of a universal stress-response genomic toolkit for animal terrestrialisation

To identify gene families that might have had an adaptive role during terrestrialisation, regardless of their age of origin, we first exposed 17 species across 7 animal phyla, including both aquatic and terrestrial species to abiotic stressors simulating some of the major environmental challenges associated with the transition from sea to land (Fig. 1b, 3a, Table S1). In brief, specimens were exposed to hypoxia, hyperoxia, UV-B (with varying recovery times), visible light, osmotic stress, and chemical cues (see Materials and Methods; (Tables S3-S19), and sequenced using RNA-seq, generating a total of 796 transcriptomic datasets. For each species, RNA material from all experimental conditions was pooled and sequenced using IsoSeq to construct a de novo transcriptome (Table S20), which was used as a reference for mapping RNA-seq reads and gene expression quantification (Tables S3-S19).

We then constructed species-specific weighted gene co-expression networks (WGCNA) based on a scale free topology (SFT) (Figures S92-S108, Table S21), identified statistically significant modules per condition (Figures S109-S125, Tables S22-S38) and extracted highly connected genes (hubs) within those modules, since hub genes are considered to play a central role in response to stress[29–31] (Tables S39-S55). Hub-containing orthogroups per species and experiment were identified by mapping the genes to the previously inferred orthogroups (see Materials and Methods) and their evolutionary origin was determined via phylostratigraphic analysis (Fig. 3b; see interactive link here: https://itol.embl.de/tree/3722324466572417463711101#), enabling comparison of gene age distributions across species. To avoid redundancy, each orthogroup was counted only once per species, regardless of multiple hub genes**.** For unbiased cross-species comparison, we calculated the proportion of hub-containing orthogroups at each branch for each species, based on the total number of hub-containing orthogroups identified in that species. We repeated the analysis for the hubs that were recovered through the proteomic analyses, as a confirmation of their translation into proteins. We then compared the proportion of hub-containing orthogroups across all experiments and species (Fig. 3c, Table S56) to reveal patterns in stress-response mechanisms associated with the transition to land.

Across all species and experimental conditions, we observed virtually no overlap in the orthogroups to which hub genes belonged—not among terrestrial species, not among aquatic species, and not even within the same phylum, except for nematodes (Fig. 3d). This pattern held

even when considering all genes within the significant modules, not just the hubs. Only 42 non hub-containing orthogroups out of the ca. 540,000 were shared across all 17 species (Fig. S126), encoding proteins of ancient origin conserved across eukaryotes and with previously identified stress-related roles, such as RAB proteins[32], selenoproteins[33], ubiquitin carboxyl-terminal hydrolase 7[34], tetraspanin[35,36], cullin[37], or putative voltage-dependent anion-selective channel[38] (Table S57). These findings indicate that stress responses have largely evolved through independent recruitment of distinct gene repertoires across lineages, rather than relying ona conserved genomic toolkit, though a small set of deeply conserved genes may underpin core functions across animals.

Despite this marked divergence at the level of gene identity, the evolutionary origins of the hub genes followed a remarkably consistent pattern. Most hub genes belonged to ancient gene families predating the emergence of terrestrial invertebrate lineages, particularly at deeper nodes up to Protostomia (Fig. 3b). Only a small fraction of hub-containing orthogroups gained after the origin of Protostomia. A few lineage-specific exceptions were found, though. For example, Onychophora showed an enrichment of hubs in orthogroups gained at the branch leading to the phylum; Nematoda exhibited a moderate proportion of hubs derived from orthogroups gained at the most recent common ancestor of Nematoidea and Panarthropoda (i.e., nematodes, nematomorphs, arthropods, tardigrades and onychophorans); Platyhelminthes showed a cluster of hubs arising in Tricladida, consistent with prior findings [20]; and the terrestrial nemertean species, along with the terrestrial arthropod species displayed species-specific gains (see interactive link here: https://itol.embl.de/tree/3722324466572417463711 01#). However, even in these cases, the majority of hubs traced back to gene families that predated terrestrialisation and originated in ancient nodes.

These results argue against a universal genomic toolkit for response to abiotic factors relative to life on land. The lack of orthogroup-level overlap among the hub genes recruited into stress-response networks suggests that different lineages independently co-opted distinct sets of genes to meet the environmental pressures associated with land colonization. Importantly, this pattern holds across both terrestrial and aquatic species and both within and between phyla, underscoring the absence of a conserved genetic solution to stress. Instead, response to abiotic stress appears to have proceeded through the lineage-specific reorganization of deeply conserved gene families into different genetic contexts. Overall, our findings support the idea that gene

reuse diminishes with increasing evolutionary divergence[39], even in response to similar abiotic stressors.

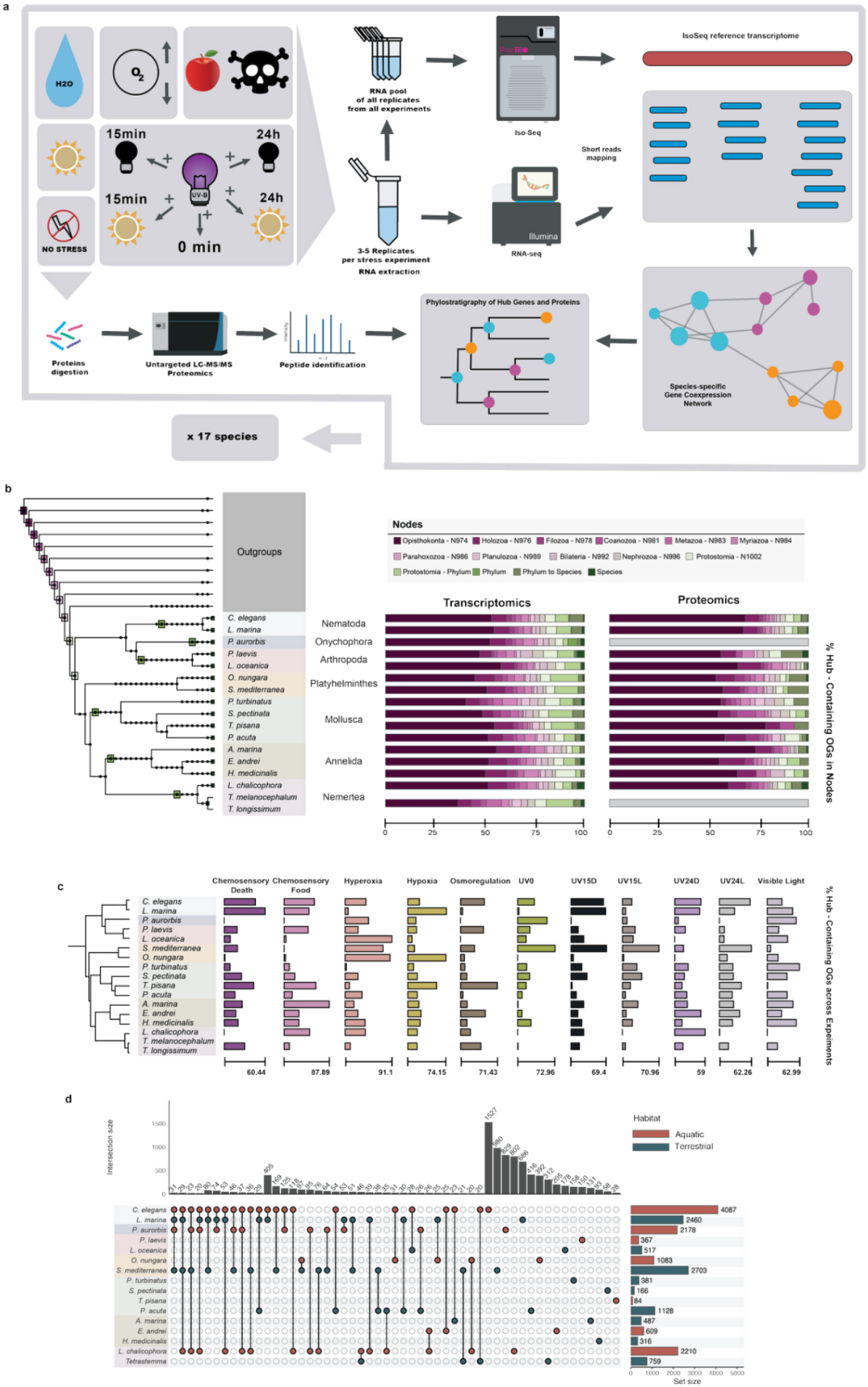
a
H2O
O2
NO STRESS
15min
24h
15min
24h
UV-B
0 min
RNA pool
of all replicates
from all experiments
3-5 Replicates
per stress experiment
RNA extraction
Iso-Seq
RNA-seq
Illumina
Short reads
mapping
IsoSeq reference transcriptome
Proteins
digestion
Untargeted LC-MS/MS
Proteomics
Peptide identification
Phylostratigraphy of Hub Genes and Proteins
Species-specific
Gene Coexpression
Network
x 17 species
b
Outgroups
C. elegans
L. marina
P. aurorbis
P. laevis
L. oceanica
O. nungara
S. mediterranea
P. turbinatus
S. pectinata
T. pisana
P. acuta
A. marina
E. andrei
H. medicinalis
L. chalicophora
T. melanocephalum
T. longissimum
Nematoda
Onychophora
Arthropoda
Platyhelminthes
Mollusca
Annelida
Nemertea
Nodes
Opisthokonta - N974
Holozoa - N976
Filozoa - N978
Coanozoa - N981
Metazoa - N983
Myriazoa - N984
Parahoxozoa - N986
Planulozoa - N989
Bilateria - N992
Nephrozoa - N996
Protostomia - N1002
Protostomia - Phylum
Phylum
Phylum to Species
Species
Transcriptomics
Proteomics
% Hub - Containing OGs in Nodes
0
25
50
75
100
c
Chemosensory Death
Chemosensory Food
Hyperoxia
Hypoxia
Osmoregulation
UV0
UV15D
UV15L
UV24D
UV24L
Visible Light
60.44
87.89
91.1
74.15
71.43
72.96
69.4
70.96
59
62.26
62.99
% Hub - Containing OGs across Experiments
d
Intersection size
1500
1000
500
0
Habitat
Aquatic
Terrestrial
Tetrastemma
4087
2460
2178
367
517
1083
2703
381
166
84
1128
487
609
316
2210
759
Set size
0
1000
2000
3000
4000
5000

204

Figure 3. Species-specific stress-response networks and ancient evolutionary origins of hub genes suggest diverse genomic routes to terrestrial life in animals. a, Overview of abiotic stress experiments, co-expression network construction and proteomic detection of hub genes across 17 species from 7 animal phyla, exposed to standardised stressors mimicking terrestrial abiotic factors. **b**, Phylostratigraphic analysis showing that the majority of hub genes originate from ancient gene families, based on genes recovered through both transcriptomic and proteomic data. Colored squares in the tree indicate the branch leading to each node, using the same color scheme as in the accompanying barplot. Nodes from collapsed branches not shown in the tree are marked with black dots. Protostomia to Phylum and Phylum to Species segments indicate the sum of all the in-between branches. Grey bars indicate missing data for specific species. **c**, Percentage of hub-containing orthogroups per species for each experiment, calculated relative to the total number of hub-containing orthogroups identified in that species. **d**, Upset plot showing overlap of hub-containing orthogroups resulted from species-specific co-expression networks. Dots connect species that have a number of hub gene orthogroups in common, the number indicated in each bar from the barplot on top. No orthogroup was shared among all terrestrial species, nor consistently within phyla, indicating lineage-specific gene recruitment. *[High resolution figure can be accessed here: https://drive.google.com/file/d/1tZoq90HS3TZlHN4yLdBqGig8CQ_SejCK/view?usp=sharing]*

Functional convergence in species-specific hub genes responding to abiotic stress

In the absence of shared orthogroups among stress-response co-expression networks across species, we next asked whether genes involved in stress response may have converged at the level of gene function. To explore this, we investigated the functional similarity of hub genes identified in co-expression networks from each species exposed to abiotic stress, applying gene ontology-based, following the approach described in[19,40] and pathway comparisons (see Materials and Methods).

In brief, we inferred GO annotation similarity across all hub-containing orthogroups per species, measured their functional similarity and grouped them into functional clusters that eventually represent functional convergence units, which we represent in what we name as constellation plots[19,40] (Fig. 4a). For each experiment, we analyzed the full hub gene set of each species in an aggregated manner and we found that hub genes across different lineages shared highly similar

functional annotations, though they belonged to entirely different gene families. When grouped by functional similarity, hub-containing gene families from different species clustered into one to four functional clusters including both aquatic and terrestrial animals, with most species always being included in a single main cluster (Fig. 4b, Fig. S127). These results suggest convergent recruitment of genes with analogous roles in abiotic stress response despite divergent evolutionary origins. This pattern was further supported by orthogroup-level clustering, which revealed that the vast majority of functional clusters comprised orthogroups containing both aquatic and terrestrial species, with only a minority of clusters showing habitat-specific composition (Tables S58-S68).

To complement these results, we examined pathway-level convergence by assessing enrichment of well-defined functional categories. Despite species-specific gene repertoires, the pathways enriched in hub gene sets under each stress condition were largely shared across species, indicating parallel recruitment of distinct gene sets into common functional frameworks. When considering all stress conditions together, a core set of conserved pathways, such as those involved in oxidative stress response, thermogenesis, metabolic regulation or signaling, emerged as recurrently enriched across lineages (Fig. 5a, Fig. S128a). However, the specific pathways activated varied depending on both the species and the type of stressor (Fig. 5b, Fig. S128b), suggesting that different lineages mobilize distinct components of these conserved functional modules in response to specific environmental challenges (See Figures S129-S139 for unfiltered list of pathways for each experimental condition).

Together, these results reveal that, while the genetic content of stress-response networks differs between species, their functional roles converged across lineages. This indicates that animals transitioning to land did not reuse the same genes, but rather recruited distinct orthogroups - most of them with an ancient evolutionary origin - to produce similar functional outcomes. Such functional convergence, emerging from non-homologous gene sets, underscores the evolutionary flexibility of gene networks and suggests that response to stress during terrestrialisation was achieved through multiple genomic trajectories leading to comparable physiological outcomes.

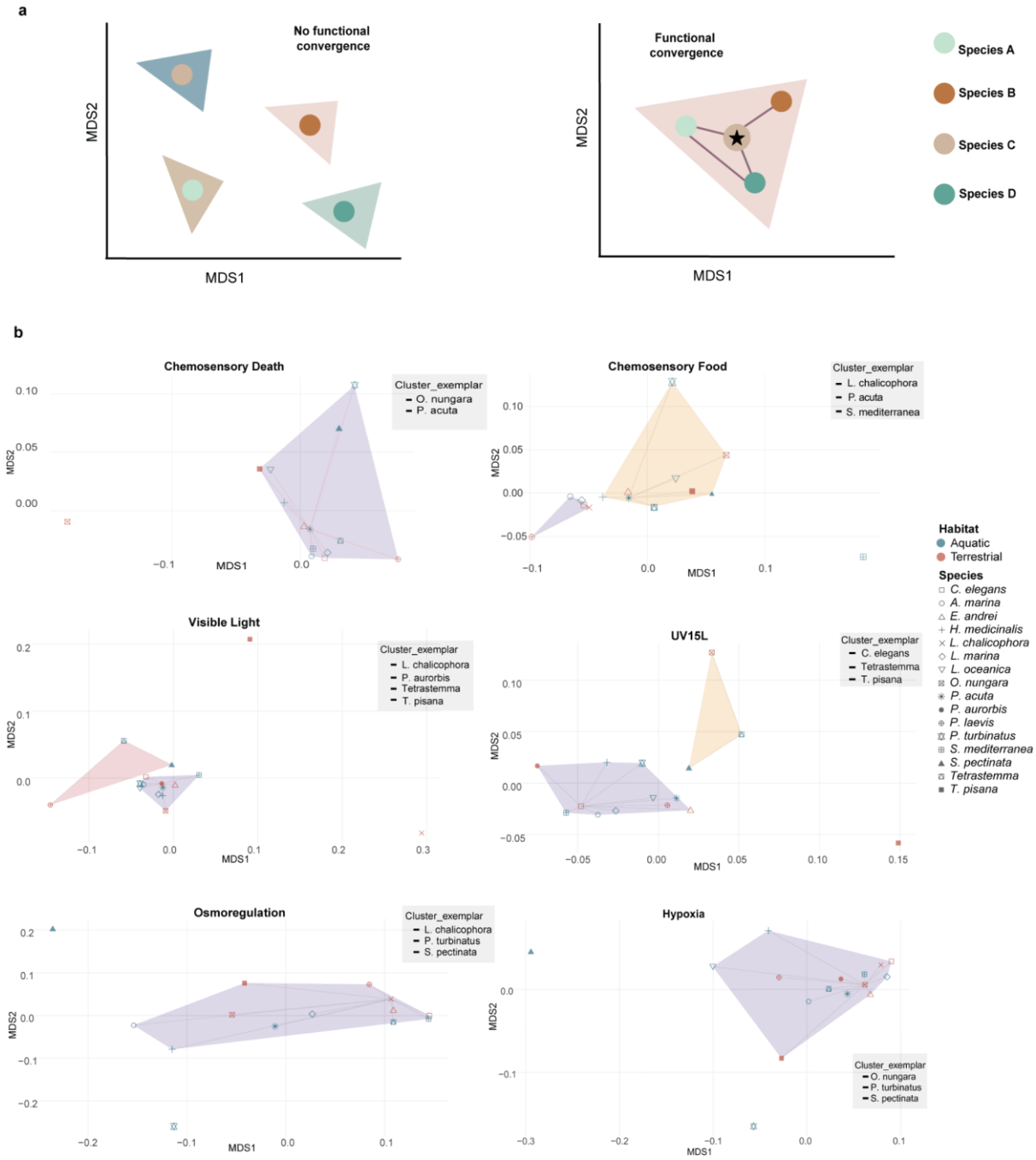

Figure 4. Functional convergence of species-specific, GO-annotated hub genes across animal lineages under stress conditions. a, Graphical illustration of constellation plots of gene functions across species. Each dot represents a species and each polygon a distinct functional cluster. On the left side each species belongs to a different cluster showing the lack of functional convergence and on the right side all species cluster together representing functional convergence. **b**, Constellation plots of functions of hub genes across 17 aquatic and terrestrial species for each experimental condition. Each polygon represents a distinct functional cluster formed by species with similar GO annotations, despite no orthogroup-level overlap across species. Cluster exemplars indicate the species that act as centroid in each cluster. The presence

of hub genes from multiple species within the same functional cluster demonstrates convergence in stress-response roles across independent lineages. Only six experiments are shown for demonstration purposes, given that all experiments showed the same pattern (see also Fig. S127) *[High resolution figure can be accessed here: https://drive.google.com/file/d/12idEuCZeijpxWJexanyAbU_KBR3Tu2Lt/view?usp=sharing]*.

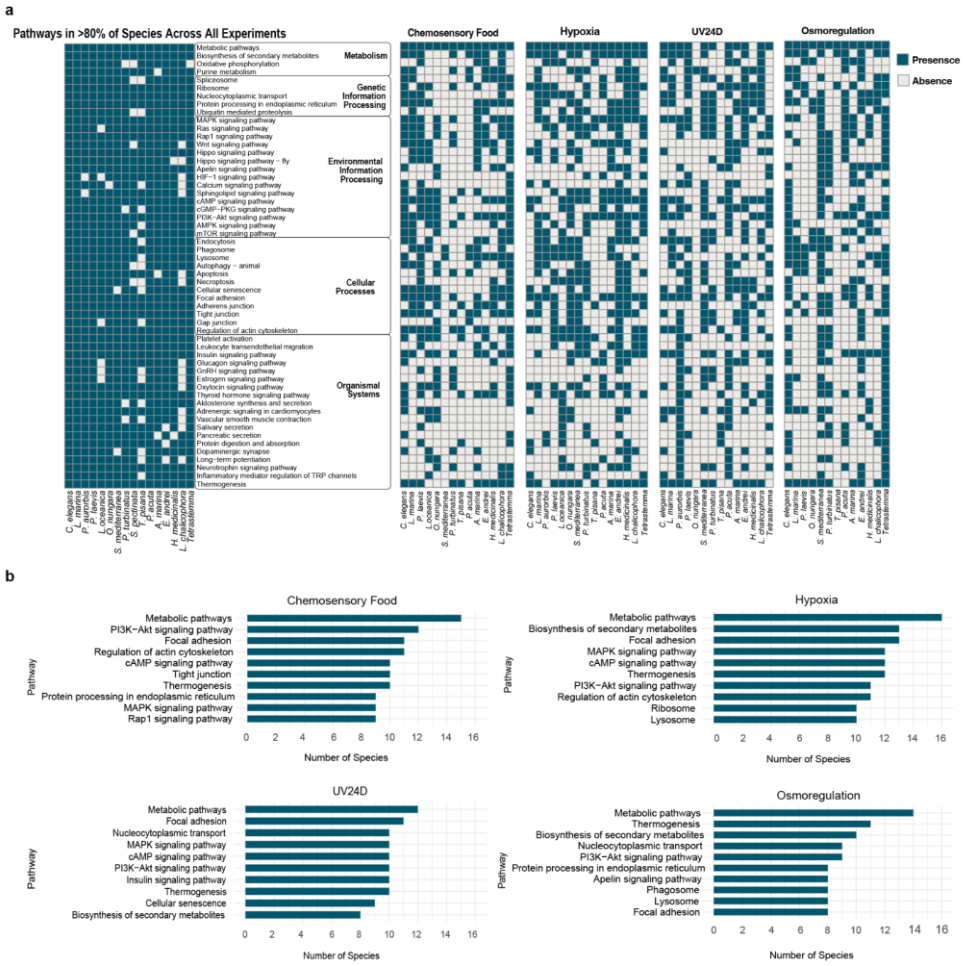

Figure 5. Functional convergence of species-specific KEGG pathways across animal lineages under stress conditions. a, Heatmaps showing the presence/absence of KEGG pathways in hub gene sets under abiotic stress conditions**.** Each row represents a KEGG pathway, and each column corresponds to a species. The left heatmap displays a summary heatmap including only pathways that are present in at least 80% of species, considering all experimental conditions combined. On the right, separate heatmaps are shown for each experimental condition, filtered by the same set of pathways (rows) as in the summary heatmap. Only four experiments are shown; all experiments showed the same pattern (see also Fig.

S128a). **b**, Top 10 pathways per experiment. The same four experiments as in 4a are shown (see also Fig. S128b). *[High resolution figure can be accessed here: https://drive.google.com/file/d/1pMzsXIEXHf6xSC4jra5MDF5YdnaYOIQN/view?usp=sharing].*

Machine learning identifies habitat-informative gene families across animal phyla

Although our stress-response experiments provide insight into how animals respond to abiotic challenges, they capture only part of the biological complexity involved in terrestrialisation—excluding major factors such as anatomical, embryological, biomechanical, or biochemical adaptations. To explore broader genomic signals potentially linked to the terrestrial habitat, we examined whether gene copy number variation could predict habitat. Gene copy number variation is a key mechanism of evolutionary adaptation, often reflecting functional shifts linked to ecological transitions[19,40,41] that often underpin physiological and functional innovations. To test this, we applied machine learning, a method that has successfully identified environment-related genes in previous studies[42,43]. We trained an XGBoost machine learning classifier using our dataset of over 500,000 orthogroups inferred for our nearly 1,000 proteomes spanning all major animal phyla, providing a kingdom-wide assessment of putative habitat-associated gene families (Fig. 6a).

Our model identified a small subset of gene families (130 orthogroups, Table S69) as the minimum number of orthogroups that accurately distinguish terrestrial from aquatic species (Fig. 6b,c). Gene family count distributions along the phylogeny showed that our model classified species based on complex patterns of copy number variation not easily assessed by eye in ancient gene families (Fig. S140-269). For example, orthogroup (OG) 8389 (Selenoprotein L, see below) is almost exclusively found in aquatic organisms (Fig. S238), while OG492 (lysosomal acid phosphatase) shows a higher count in some terrestrial lineages than their aquatic relatives, but the opposite trend in others (Fig. S169). This suggests that complex gene duplication and loss dynamics of ancient genes could have contributed to the transition of animals to life on land. Importantly, the discriminative power of these orthogroups does not arise from simple presence or absence or congruent expansions and contractions in independent terrestrial lineages, but from lineage-specific shifts in gene family size, reflecting diverse, independent, and complex evolutionary trajectories that led to convergent adaptation to terrestrial environments.

Functional annotation of these habitat-informative orthogroups revealed gene families involved in processes relevant to environmental stress, metabolism, signaling, and development (Fig. 6d, Table S69), comprising metabolic enzymes, ion and solute transporters, and odorant receptors, which share functional roles with, or are themselves, gene families previously linked to terrestrialisation[19–23,44], among others. Known gene families include the cytochrome P450s (CYP450s) and flavin-containing monoxygenases (FMOs), involved in the detoxification of xenobiotics, cellular metabolism, and homeostasis. Both were parallelly expanded in independent mollusc out-of-the-sea transitions[19]. CYP450s were also previously associated with critical functions during plant transition to land[45], while FMOs are involved in the metabolism of Trimethylamine[46], characterised by its strong fish-like odor. OG6 (serine proteases) includes vertebrate coagulation factors, one of which (factor XII) emerged before the appearance of lungfishes, during the tetrapod water-to-land transition, and has been hypothesised to confer adaptive advantages by enabling rapid clotting in soil-contaminated wounds, mitigating infection and blood loss in the terrestrial environment[47]. Other less-studied gene families identified as relevant for animal terrestrialisation were Rapunzel-like, which participates in skeletal and muscular development in fish but is absent in tetrapods[48], and Selenoprotein L, whose function remains unknown, but was predicted in our functional analysis to be involved in chromosome segregation. The latter protein incorporates the rare amino acid selenocysteine, which depends on environmental selenium for its synthesis. It has been hypothesised that the greater bioavailability of selenium in aquatic environments, along with the increased oxidative stress associated with higher oxygen levels on land, has led aquatic species to retain larger selenoproteomes than their terrestrial counterparts[49,50], highlighting a potential link between terrestrialisation, oxygen availability, and selenoprotein evolution. Transport of ions and solutes, such as trehalose, involved in osmoregulation, was also represented in the identified gene families. These functions are broadly consistent with the physiological demands of land life, including coping with oxidative damage, managing dehydration and oxygen variability, and processing novel chemical cues.

We further evaluated the overlap between those habitat-informative orthogroups and the hub genes previously identified in species-specific co-expression networks derived from transcriptomic experiments. Out of the 130 total orthogroups identified through machine learning, 80 contained hub genes from at least one species (Fig. 6a). This overlap suggests that gene families whose copy number variation correlates with habitat may also contribute to real-time transcriptional responses to environmental challenges. However, these orthogroups account

for only a subset of the total hub gene repertoire, and their involvement as hubs is not consistent across species, even when the gene families are broadly conserved, underscoring the role of species-specific genomic rewiring in shaping stress responses.

Taken together, these results highlight a small but functionally relevant set of gene families that have undergone recurrent copy number shifts associated with habitat transitions, reflecting parallel evolutionary responses to ecological change. Moreover, their dual roles as predictive features of habitat and as transcriptional hubs suggest that these genes represent flexible genomic elements that might have been co-opted into the physiological response to stress or other challenges posed by terrestrial life.

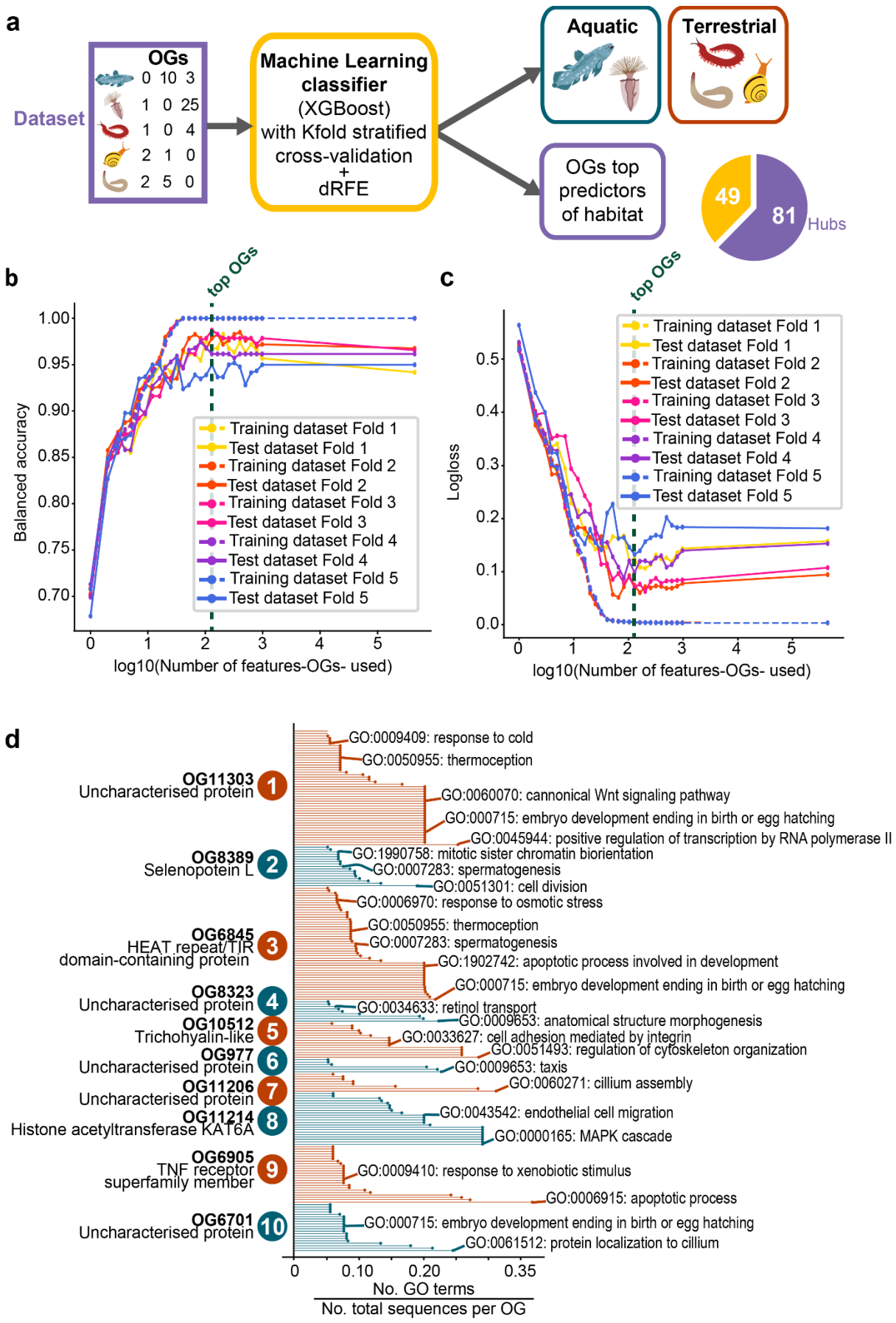
a
Dataset
OGs
0 10 3
1 0 25
1 0 4
2 1 0
2 5 0
Machine Learning classifier
(XGBoost)
with Kfold stratified cross-validation
+
dRFE
Aquatic
Terrestrial
OGs top predictors of habitat
49
81
Hubs
b
top OGs
Balanced accuracy
log10(Number of features-OGs- used)
Training dataset Fold 1
Test dataset Fold 1
Training dataset Fold 2
Test dataset Fold 2
Training dataset Fold 3
Test dataset Fold 3
Training dataset Fold 4
Test dataset Fold 4
Training dataset Fold 5
Test dataset Fold 5
c
top OGs
Logloss
log10(Number of features-OGs- used)
d
OG11303 Uncharacterised protein 1
OG8389 Selenopotein L 2
OG6845 HEAT repeat/TIR domain-containing protein 3
OG8323 Uncharacterised protein 4
OG10512 Trichohyalin-like 5
OG977 Uncharacterised protein 6
OG11206 Uncharacterised protein 7
OG11214 Histone acetyltransferase KAT6A 8
OG6905 TNF receptor superfamily member 9
OG6701 Uncharacterised protein 10
GO:0009409: response to cold
GO:0050955: thermoception
GO:0060070: cannonical Wnt signaling pathway
GO:000715: embryo development ending in birth or egg hatching
GO:0045944: positive regulation of transcription by RNA polymerase II
GO:1990758: mitotic sister chromatin biorientation
GO:0007283: spermatogenesis
GO:0051301: cell division
GO:0006970: response to osmotic stress
GO:0050955: thermoception
GO:0007283: spermatogenesis
GO:1902742: apoptotic process involved in development
GO:000715: embryo development ending in birth or egg hatching
GO:0034633: retinol transport
GO:0009653: anatomical structure morphogenesis
GO:0033627: cell adhesion mediated by integrin
GO:0051493: regulation of cytoskeleton organization
GO:0009653: taxis
GO:0060271: cillium assembly
GO:0043542: endothelial cell migration
GO:0000165: MAPK cascade
GO:0009410: response to xenobiotic stimulus
GO:0006915: apoptotic process
GO:000715: embryo development ending in birth or egg hatching
GO:0061512: protein localization to cillium
No. GO terms
No. total sequences per OG

370

Figure 6. Machine learning identifies 130 orthogroups (OGs) predictors of habitat. a, Simplified workflow of machine learning analysis. The pie chart shows the number of OGs from the top 130 that contain hubs from stress-related modules in GCN. **b**, Balanced accuracy for each model trained across all iterations of the dRFE workflow for training and testing datasets of all folds. The dashed dark green line shows the iteration where we select the top OGs. **c**, Logloss values for each model trained across all iterations of the dRFE workflow for training and testing datasets of all folds. The dashed dark green line shows the iteration where we select the top OGs. **d**, Functions from the top 10 OGs as ranked by the machine learning model. OG name was obtained with BLASTp. GO terms on the right were predicted using FANTASIA. Full GO terms in Fig. S270, Table S69. *[High resolution figure can be accessed here: https://drive.google.com/file/d/1CEA6lNXzufhE94N_xZdgMPYCUku3IAa0/view?usp=sharing].*

Discussion

The repeated emergence of terrestrial life across animal phyla is without doubt one of the most remarkable examples of repeated evolution in the animal evolutionary chronicle. Whether such independent ecological transitions might have been facilitated by common or lineage-specific genomic changes has never been addressed. Our results provide evidence of a lineage-specific reshaping of the genetic repertoire, coupled with a rewiring of the genomic responses to key abiotic stressors encountered during terrestrialisation, achieved largely through the co-option of ancient gene families. Despite the lack of shared orthologs central to stress response across lineages, concordant with the expectation of reduced gene reuse as divergence times increase [39], we observed functional convergence in the functions and pathways of independently recruited stress-response genes. In addition, we identified a small subset of shared ancient and conserved gene families, primarily involved in stress responses, metabolism, and development, that might have contributed to terrestrial adaptation through a complex pattern of gain, duplication and loss.

Rather than relying on novel genes, such as stress response in yeasts[51], or the repeated acquisition of the same genetic element, such as the parallel loss of an enhancer causing pelvic reduction in stickleback fish[52], the emergence of terrestrialisation seems to depend on the inherent plasticity and modularity of the pre-existing gene repertoire, in line with the classical idea of "evolution as a tinkerer"[53]. Previous studies have shown this trend on plant[29–31], vertebrate[22], mollusc[19], and flatworm[20] terrestrialisation, and on the response to desiccation in

gecarcinid land crabs[54]. In this framework, ancient gene families serve as a reservoir of functional potential that can be differentially co-opted into pre-existent genetic networks in response to different ecological contexts, as previously shown for nutrient response gene regulatory networks in plant terrestrialisation[55]. Alternatively, the loss of genes integrated in pre-existent networks, even central ones, and the incorporation of new genes can also facilitate adaptation[56–58]. All this, together with our results, highlights the importance of considering systems-level properties, such as co-expression network architecture, hub gene centrality, and pathway redundancy, when investigating the genomic basis of adaptation and convergent evolution.

While our present-day stress experiments and phylogenomic approach cannot recapitulate the full complexity of terrestrialisation, limited in part by the lack of experimental resources available for non-model invertebrate organisms, they provide the first comparative approach to understand how completely different animals could have independently reshaped their gene repertoire to cope with terrestrial life. Our results offer a perspective on how life repeatedly overcomes the challenges of novel environments not by inventing entirely new solutions, but by tinkering ancient ones.

Materials and Methods

Species selection for kingdom-wide gene repertoire evolutionary dynamics

We selected 960 animal species covering all animal phyla, and 13 outgroup species (Table S1). We paid special attention to their taxonomic distribution to ensure that internodes leading to terrestrial lineages were well represented. Per-gene protein sequences were obtained from MATEdb2[59]. For each species, the longest isoform per gene was parsed for orthology inference. Reference transcriptomes from species collected to carry out abiotic stress experiments were added as well (see below). Information on the source data type for each species (i.e. genome, RNA-seq transcriptome or IsoSeq transcriptome) can be found in Table S1. We grafted our species tree based on the information available in the literature.

Species tree topology sources

Deep relationships between animal phyla are still the topic of debate in the scientific community. For our species selection, we decided to use the most recent and sound phylogenomic studies

whenever possible. The use of alternative topologies to the one considered here for these unresolved relationships would not affect the general conclusions of our results, as terrestrialisation events occurred later and most gene families that we discussed originated before these events (regardless of the specific timing of origin).

For the most recent interrelationships, there were some cases where only a few markers or even morphological studies that include those species existed. There were a few cases where information on the exact relationship between three or four species was not available (i.e., Talitridae -Arthropoda-, *Siphonaria* -Mollusca-, Nerididae -Annelida-, Opilioacarida (Arthropoda), Sesarmidae (Arthropoda), Hyppolytidae (Arthropoda)), forming a polytomy that was resolved using ETE v3.1.2[60]. These should not affect the conclusions, either, as our results suggest a higher importance for ancient genes that predate these branches.

For several terrestrial lineages (e.g., Talitridae, Amphipoda), only genomic or transcriptomic data of a single terrestrial species were available. This would affect our results in the sense that we would not be able to distinguish between lineage- and species-specific gene families. For this reason, these cases were not considered for the gene repertoire evolution analyses.

Methods Table 1. Species phylogeny topology sources per lineage/group.

Lineage/clade/group of species	Reference(s)
Outgroups	61
Metazoa backbone	62
Porifera	63,64,65
Cnidaria	66,67
Acoela	68
Echinodermata	69
Hemichordata	70

Lineage/clade/group of species	Reference(s)
Cephalochordata	71
Craniata Actinopterygii Amphibia	72,73 74–76 77
Ecdysozoa	78,79
Kinorhyncha	80
Nematoda *Litoditis* + *Oscheius* Tylenchina + Panagrolaimidae	81 82 83
Nematomorpha	84
Tardigrada Macrobiotidae Richtersiidae	85–88 89 90
Onychophora *Eoperipatus*	91 92
Arthropoda Chelicerata Astigmata Trombidiformes Pseudoscorpiones Araneae Myriapoda Lithobiomorpha Scutigeromorpha Pancrustacea Oligostraca + Malacostraca + Branchiopoda Myodopida + Podocopida	93 94 95 96 97 98 99 100 101 102 103 104

Lineage/clade/group of species	Reference(s)
Podocopida +Cypridocopida	105
Notostraca + Spinicaudata	106
Lepidurus triops	107
Malacostraca	102
Amphipoda	108
Pardaliscidae	109
Tanaidacea	110
Isopoda	111,112
Asellidae	113
Paraplatyarthrus subterraneus	114
Euphausiacea	115
Decapoda	116
Caridea	117
Sergestidae	118
Anomura	119
Brachyura	120
Thoracotremata	121
Hexapoda	122
Collembola	123
Entomobryomorpha	124
Tomocerinae	125
Diplura	126
Protura	127
Insecta	122
Blattodea	128
Paraneoptera	129
Coleoptera	130
Lepidoptera	131
Hymenoptera	132
Diptera	133
Protostomia	

Lineage/clade/group of species	Reference(s)
Cycliophora	[134]
Dicyemida	[135]
Spiralia	[136] (Fig. S1)
Chaetognatha	[137]
Rotifera	[138]
Platyhelminthes	[139,140]
Bryozoa	[141,142]
Entoprocta	[143]
Mollusca	[144,145]
Polyplacophora	[146]
Caudofoveata + Solenogastres	[147]
Cephalopoda	[148–150]
Gastropoda	[151]
Neomphalida	[152]
Vetigastropoda	[153]
Patellogastropoda + Neritimorpha	[154–156]
Caenogastropoda	[157,158]
Nudibranchia	[159]
Panpulmonata	[160]
Helicidae	[161]
Arion vulgaris + *Meghimatium*	[162]
Ampullaridae	[157]
Bivalvia	[163]
Unionida	[164]
Mytilida + Ostreoidea	[165]
Ostreidae	[166]
Annelida	

Lineage/clade/group of species	Reference(s)
Early-splitting annelids + Sedentaria	167
Siboglinidae	168
Oasinia alvinae	169
Spinther	170
Sipuncula	171
Errantia	172
Aciculata	173
Dimorphilus + Sedentaria	174
Sabellida	175
Terebelliformia	176
Clitellata	177
Whitmania pigra	178
Nemertea	179
Hoplonemertea	180
Lineidae	181
Brachiopoda	182,183
Phoronida	184

Extant and ancestral habitat reconstruction

Habitat information for each species was mostly obtained from the World Register of Marine Species (WoRMS) database [185] (last accessed in January 2023). To simplify, a species was considered terrestrial if it spent at least one stage of its life cycle in a terrestrial environment. The only exceptions were the diving bell spider, *Argyroneta aquatica*, and the maritime centipede, *Strigamia maritima*, which were considered terrestrial because they conserve most adaptations to life on land.

We inferred the ancestral habitat of each branch using the R package paleotree v3.4.7[186] using the MPR method, which provided a reconstruction more congruent with the literature than the ACCTRAN method. For ambiguous and wrongly assigned branches (Fig. S271), we manually

assigned the habitat to aquatic (Fig. S272). The purpose of this analysis was to plot in the main figures. Results were not used for any additional analyses.

MPR gives ambiguous reconstructions in 3 lineages: nematodes, molluscs, and annelids. For nematodes, no paper infers the ancestral habitat state. One paper suggested more than 30 transition events (Holterman et al., 2019), but they did not distinguish between terrestrial and freshwater. The ambiguous group in question (Plectida) includes terrestrial and aquatic (marine) clades (supplementary figure 1 in that paper), making it more likely that the ancestor was aquatic. More specifically, we can say that branch 1116 from our tree is most likely aquatic, while 1117 could also be terrestrial. For molluscs, we used the habitats previously inferred[160]. For annelids, we used the habitats previously inferred[177]. One species (*Drawida*) was considered as part of Crassiclitellata in their ancestral reconstruction, but not in their final selected topology. So, we considered this as a putative secondary terrestrialization event and left the ancestor as aquatic, in the absence of additional evidence that favored one of the two options.

In addition, we are also getting results inconsistent with known information from the literature. MPR considered the ancestor of all arthropods and tardigrades to be terrestrial. This was changed to aquatic.

Gene repertoire evolutionary dynamics analyses

We used SonicParanoid2 v2.0.8 (fast mode[187] to reconstruct orthologous groups (orthogroups) in our 973 species. A total of ~20M protein-coding sequences were clustered into 514,979 OGs, while ~5M were left unclustered. OGs were used as a proxy for gene families and used to infer gene gains and losses at different nodes using ETE v3.1.2[60]. For gains, we identified the most recent common ancestor (MRCA) of all OGs to determine the age of origin of each OG. For losses, we used a modification of the custom script used in[174] (see 'Code availability'). In brief, a gene loss was inferred at a given node whenever a specific OG contained no sequences from all the species that belonged to that clade.

Functional enrichment analyses

We downloaded FANTASIA v1[188] GO functional predictions, based on similarity of embeddings from protein language models, from MATEdb2[59] or ran new inferences for the newly IsoSeq sequenced species.

To identify the function of OGs that were gained or lost at the origin of terrestrialisation lineages (containing at least two terrestrial species), we performed a GO enrichment of the proteins contained within those OGs from selected species. For each node, we selected the smallest number of species necessary to ensure complete OG representation. For gene gains, species were selected from within the clade defined by the node. For gene losses, species were selected from the sister lineage to the clade of interest (e.g., remipedes for Hexapoda). In Myriapoda and Onychophora, where including all species was unfeasible, we ranked species by the number of OGs they contained, and selected the top 25. This subset recovered over 50% of the OGs, as shown by the cumulative increase in OGs with each added species (Fig. S91c, d). For each terrestrialisation node, we performed separate GO enrichment analyses with topGO[189] for gene gains and losses. In both cases, the GO enrichment analyses were first done per species using the full proteome of that species as the background. We then combined the p-values using the ordmeta method [190] to identify enriched GO terms for genes gained or lost at the terrestrialisation node. Functional convergence was also assessed as explained below (see 'Functional convergence' section).

Stress experiments and RNA sequencing, and preprocessing

To pinpoint the gene repertoire composing the terrestrialisation genetic toolkit, we selected 17 aquatic and terrestrial species spanning 7 animal phyla (Annelida, Platyhelminthes, Nemertea, Mollusca, Arthropoda, Onychophora, and Nematoda) (Fig. 1b, Table S70). We collected and used between 19 and 68 specimens per species to carry out the abiotic stress experiments detailed below (excepting in nematodes, where several specimens were pooled to do the experiments due to their microscopic size) (Tables S3-S19). Due to constraints in specimen availability, age and sex were neither assessed nor controlled; individuals were used as collected, regardless of developmental stage or sex. The intensity and duration of each stressor were calibrated to elicit a genetic response without causing mortality, ensuring that the conditions fell within a biologically relevant range to reveal the gene repertoire underlying abiotic stress adaptation.

Natural light – Terrestrial species are regularly exposed to visible light as part of their daily environmental conditions, while many aquatic invertebrates typically experience limited or no direct light exposure. This ecological contrast suggests that light may act as a more frequent and biologically relevant stressor in terrestrial environments. To assess differential responses to visible light across aquatic and terrestrial species, we exposed individuals from all taxa to ambient natural light for 15 minutes prior to dissection and flash freezing (experiment code: VL). This allowed us to identify light-induced transcriptional responses and assess whether visible light exposure elicits distinct gene expression patterns that may reflect lineage-specific physiological adjustments associated with life on land.

Protection against UV radiation – Ultraviolet (UV-B) radiation (280–315 nm) is a potent genotoxic stressor that induces DNA damage primarily through the formation of cyclobutane pyrimidine dimers and 6–4 photoproducts[191]. These lesions cause structural distortions in the DNA helix, disrupting both transcription and replication. Two of the major repair pathways animals have evolved to mitigate such damage are: photoreactivation (light-dependent), which directly reverses DNA lesions using photolyase enzymes[192], and nucleotide excision repair (NER, or "dark repair"), a light-independent mechanism that removes damaged nucleotides through excision and resynthesis[193]. To investigate UV-induced stress responses and the dynamics of DNA repair, specimens were exposed to UV-B radiation (302 nm) at 8.48 W/m² using a UVM-28 EL Series UV lamp (Analytik Jena US) for durations ranging from 30 seconds to 3 minutes, depending on species-specific tolerance (see Supplementary Table S72). Following exposure, animals were either flash-frozen immediately (experiment code: no recovery, UV0), or allowed to recover for 15 minutes or 24 hours under either visible light (experiment codes: UV15L, UV24L) or darkness (experiment codes: UV15D, UV24D). This design enabled us to distinguish between immediate damage responses and downstream repair mechanisms, and to experimentally separate light-dependent and light-independent pathways of DNA repair.

Osmoregulation experiments – Successful transition from marine to terrestrial environments requires major physiological adaptations in water balance regulation. Among the most critical challenges for terrestrial animals is the risk of dehydration due to increased evaporative water loss in air[194]. To assess desiccation tolerance in terrestrial species, we reduced ambient relative humidity to 29–30% RH and placed individuals in petri dishes where surface moisture was removed using filter paper, a fine brush, or silica gel beads, depending on the species' morphology. Behavioural and morphological indicators of dehydration, such as reduced activity

or loss of cuticular shine, were carefully monitored, and the experiment was terminated once early signs of desiccation became apparent. In aquatic species, we examined osmoregulatory capacity by exposing marine animals to freshwater and freshwater animals to seawater for 30 seconds to 2 minutes, depending on species-specific tolerance (see Table S72 for conditions). These treatments simulate abrupt osmotic shifts and allowed us to characterise gene expression responses associated with maintaining ionic and water homeostasis—key processes likely to be involved in the evolution of terrestrial life.

Oxygen pressure experiments – One of the major physiological barriers to terrestrialisation is the shift from extracting oxygen in water to breathing air, which involves coping with different oxygen solubility and availability. To simulate this transition, we exposed animals to controlled oxygen extremes that reflect the lowest and highest oxygen concentrations known to support life in aquatic and terrestrial environments[195,196]. Hypoxic conditions were generated using a HypoxyLab™ Hypoxia chamber (Oxford Optronix), except for Onychophora, where helium gas displacement was used as an alternative method due to logistic constraints during the field expedition. For hyperoxia, pure oxygen (ClearO2, UK) was sprayed into airtight glass containers until the target oxygen concentration was reached. Oxygen levels were continuously monitored using an OXY-1 SMA Single Channel Fiber Optic Oxygen Transmitter (PreSens Precision Sensing GmbH) and Planar Oxygen-Sensitive Spots affixed inside the experimental chambers. In hypoxia experiments, terrestrial animals were placed directly into airtight glass containers, which were then inserted into the HypoxyLab to achieve oxygen concentrations between 13–15% O_2. For aquatic species, the containers were pre-filled with seawater or freshwater (depending on the species), and the oxygen concentration was reduced to 8% O_2 before animals were introduced. For hyperoxia, terrestrial animals were transferred into pre-equilibrated airtight chambers after spraying with pure oxygen to achieve 40–42% O_2. Oxygen levels were maintained by additional injections as needed. In aquatic species, water was pre-oxygenated to reach 42–45% O_2 before animals were added. All exposures were conducted for 20 minutes to ensure sufficient physiological engagement without causing harm.

Reception of chemical cues – The transition from aquatic to terrestrial environments necessitated profound changes in sensory systems, particularly in the detection and processing of chemical cues. While chemosensation is a universal mechanism across animals, the nature of chemical stimuli differs markedly between water and air, requiring lineage-specific adaptations in receptor types and signaling pathways. To investigate how aquatic and terrestrial invertebrates

respond to ecologically relevant chemosensory cues, we designed experiments using both attractive and aversive stimuli. For attractive cues, individuals were exposed to food sources representative of their natural diet (see Table S72 for species-specific details). To simulate warning signals, we used decomposition-associated fluids. In brief, one conspecific individual per species was euthanised and allowed to decompose in phosphate-buffered saline (PBS), freshwater, or seawater, depending on the organism's native environment. The resulting fluid (dead conspecific) was used as an aversive chemosensory stimulus (experiment code: CD, chemosensory death). During trials, live specimens were placed individually in petri dishes—either dry or containing a small volume of water—while the stimulus (food or decomposed fluid) was introduced at the center. Behavioral responses, such as approach or avoidance, were monitored in real time. Upon a clear reaction (e.g., attraction or withdrawal), the experiment was concluded, and the sample was flash-frozen for RNA extraction.

For each treatment, we used several biological replicates per taxon and included a negative control (see Tables S3-S19 for detailed description). Specimens were flash frozen immediately after each experiment. In the case of onychophorans, samples were kept in RNAlater or TRIzol at -70ºC until processed. For small animals (for instance nematodes, nemerteans and molluscs), RNA was extracted from the whole specimen. For medium-sized specimens (as annelids or onychophorans), they were dissected into anterior and posterior parts (see Table S3-S19 for detailed description on replicates). RNA extractions after stress experiments were performed using the TRIzol® reagent (Invitrogen, USA) method following the manufacturer's instructions and using MaXtract® High Density tubes (Qiagen) to minimize DNA contamination prior to mechanical sample homogenization either by plastic rotor pestles or by ceramic mortar, depending on the sample. The concentration of all samples was assessed by Qubit RNA BR Assay kit (Thermo Fisher Scientific). Libraries were prepared with the TruSeq Stranded mRNA library preparation kit (Illumina), and sequenced on a NovaSeq 6000 (Illumina, 2 × 150 bp) for a minimum of 6Gb coverage. Summary statistics of sequenced data are shown in Table S3-S19.

Because most animal species do not yet have sequenced genomes, and high-quality transcriptomes have been shown to sufficiently capture gene repertoire evolutionary dynamics, particularly when completeness metrics such as BUSCO scores are high[197], we generated full-length transcriptomes as reference datasets for co-expression network analysis. The same RNA extractions used for short-read sequencing were pooled together in each species to prepare an IsoSeq library. RNA samples were subjected to DNAse treatment using the Turbo DNA-free

DNase (Invitrogen) following the manufacturer's instructions. SMRTbell libraries were generated following the procedure 'Preparing Iso-Seq® libraries using SMRTbell® prep kit 3.0 (PN 102-396-000 REV02 APR2022)'. To enable pooling of multiple samples on 1 SMRTcell, libraries were made using barcoded adapters. The libraries were sequenced on a Sequel-IIe using Sequel II sequencing kit 2.0 and Binding kit 3.1 with 24 hr movie-time. Summary statistics of sequenced data is shown in Table S20. For the mollusc *Siphonaria pectinata*, due to the failure to successfully prepare an IsoSeq library, we built a reference transcriptome with Trinity v2.11.0[198] using 2 replicates per experiment condition and proceeded with the MATEdb2[59] pipeline.

Raw Illumina RNA-seq reads for all the experiments and species mentioned above were preprocessed using Trimmomatic v0.11.9[199] by removing adapters and ambiguous bases (MINLEN: 75, SLIDINGWINDOW: 4:15, LEADING: 10, TRAILING: 10, AVGQUAL: 30). Both raw and trimmed reads were assessed using FastQC (https://www.bioinformatics.babraham.ac.uk/projects/fastqc) before any further analysis. For IsoSeq data, the data was demultiplexed with the IsoSeq pipeline v4.0.0 (https://github.com/PacificBiosciences/pbbioconda), and cDNA primers were removed using LIMA v2.7.1. PolyA tails and artificial concatemers were removed using isoseq refine v4.0.0, and the Full Length Non Concatemer (FLNC) reads were clustered into the final de-novo reference transcriptome using CD-HIT v4.8.1 (cd-hit-est, a=0.99)[200]. Each species-specific high-quality full-length reference transcriptome was evaluated using BUSCO (v5.4.7) using as reference database metazoa_odb10[201], with all reference transcriptomes showing very high BUSCO values (Table S20), hence being of enough quality to proceed with downstream analyses. Reference transcriptomes were translated into proteins using TransDecoder v5.5.0 (https://github.com/sghignone/TransDecoder), decontaminated using BlobTools v2 (https://blobtoolkit.genomehubs.org/blobtools2/), and the longest isoforms were obtained using a custom script for further functional analyses. The longest isoform proteomes were used as input in the orthology inference (see below).

Gene co-expression network construction

For each species, trimmed Illumina RNA-seq reads from each experiment were quasi-mapped to the corresponding species-specific IsoSeq transcriptome using Salmon v1.10.2[202]. Genes were filtered to retain only those with ≥10 counts in at least 90% of samples across all

experiments, ensuring data sparsity did not confound network construction. Expression values were transformed using the regularised log (rlog) method implemented in DESeq2 v1.44.0[203], which stabilizes variance across expression levels and is recommended for gene co-expression analysis. Batch effects were estimated and removed using the removeBatchEffect() function from limma v3.60.6[204], with automatic detection of hidden batch structure via surrogate variable analysis. Data integrity was assessed by identifying and excluding low-quality genes and outlier samples using the goodSamplesGenes() function from WGCNA v1.73[205]. Additional quality checks included principal component analysis and sample clustering via heatmaps (Figures S273-289), performed using the plot_PCA() and plot_heatmaps() functions from BioNERO v1.12.0[206], prior to network construction.

Gene co-expression networks were independently constructed for each species with Weighted Gene Co-expression Network Analysis (WGCNA) using the reads generated by stress experiments. The soft-thresholding power β was determined using the pickSoftThreshold() function, with biweight midcorrelation (bicor) and a *signed hybrid* network type to fit the scale-free topology, at the threshold of $R^2 \geq 0.8$. The mean connectivity and scale-free topology fit were visualised using softConnectivity() and scaleFreePlot() to confirm the scale-free topology of the constructed networks. Networks were constructed using the blockwiseModules() function (*signed TOMType = signed, networkType = signed hybrid , deepSplit = 4, minModuleSize =30, mergeCutHeight = 0.15*), and module color assignments were extracted for downstream analysis.

To identify significant modules and extract hub genes, we first filtered co-expression modules based on their correlation with traits of interest (stress experiments), retaining only those with significant associations (p-value < 0.05). Hub genes were then extracted by selecting genes with both high gene significance (|GS| > 0.2) and high intramodular connectivity (|KME| > 0.8) within the significant modules and used for further analysis.

Proteomic validation of abiotic stress-induced hub genes

We performed untargeted LC-MS/MS proteomics to characterize proteins present in each species from those included in the abiotic stress experiments, using the control samples (see above). Samples were digested with TRIzol® reagent (Invitrogen, USA) and the protein phase was isolated, following the protocol in[207]. Samples were reduced with Tris (2-carboxyethyl)

phosphine (100 mM, 60 ºC, 30 min) and alkylated in the dark with iodoacetamide (20 mM, 25 ºC, 30 min). The resulting protein extract was acidified with phosphoric acid. Trypsin digestion and cleanup were performed according to the S-Trap manufacturer's instructions. Briefly, samples were loaded on S-Trap micro spin columns (ProtiFi, LLC cat # C02-micro) and washed extensively with 90% methanol containing 100 mM TEAB, pH 7.55. Trypsin was added directly to the microcolumn (1:10 w:w, 37ºC, 8h, Promega cat # V5113) and then peptides were eluted by serial addition of 50 mM TEAB, 0.1% formic acid, and 0.1% formic acid in 50% acetonitrile. Protein extracts were analysed on an Orbitrap Fusion Lumos mass spectrometer coupled to an EASY-nLC 1200 system. Peptides were separated via reverse-phase chromatography over a 50-cm C18 column, using a linear acetonitrile gradient. Data were acquired in data-dependent acquisition mode with dynamic exclusion, and spectra were searched using the Mascot engine v2.6 against species-specific de novo assembled transcriptomes.

Protein identification was based on high-confidence peptide matches with a false discovery rate (FDR) of ≤1% in Protein Discoverer v2.5. Only master proteins supported by unique peptides were retained, and the homogeneity of replicates was assessed by checking the percentage of proteins present in at least 2 replicates (Table S71). Quality control was ensured via regular BSA injections and QCloud performance monitoring[208]. Further experimental details follow those described in[207].

Phylostratigraphic analysis of hub genes

To reconstruct the evolutionary history of hub genes, we mapped the experimentally identified, species-specific hub transcripts from each condition to their corresponding proteins in the reference proteomes and assigned them to orthogroups for phylostratigraphic analysis using custom scripts (see 'Code availability'). Since each species had a different number of hub genes and these linked to varying numbers of orthogroups, we normalised the data by calculating percentages, i.e., dividing the number of genes assigned to each phylostratum (Node) by the total number of hub genes per species. This approach ensured comparability across species and prevented bias due to differences in gene set sizes. The same approach was followed with hub genes corroborated by proteomics. Results were visualised with iTOL v7[209]. RNA-seq data from *T. melanocephalum* and *T. longissimum* were merged at the genus level (*Tetrastemma*) because insufficient specimens were available from a single species to perform all stress experiments; as a result, different experiments were conducted on each of the two species.

The intersection of hub-containing orthogroups between species and experiments was calculated and visualised with upset plots using the R package ComplexUpset v1.3.3[210] with 'exclusive_intersection' (i.e., distinct) mode.

Functional annotation of the 42 non-hub containing orthogroups shared across all species exposed to environmental stressors was performed with BLASTp against the NCBI non-redudant protein database and KEGG pathway annotation was performed with KEGG Mapper[211] and BlastKOALA[212]. The annotation was conducted using all the genes of *C. elegans* present in those 42 orthogroups as representative.

Functional convergence

To explore potential functional convergence between hub genes orchestrating the transcriptomic response to the different environmental species in each species, we employed two strategies.

The first strategy involved generating "constellation plots" using the R package constellatoR v0.1.0)(https://github.com/MetazoaPhylogenomicsLab/constellatoR) from pre-computed "Biological Process" GO terms semantic similarity matrices. We created a custom script that used pygosemsim (https://github.com/mojaie/pygosemsim; same GO release as FANTASIA: March 22nd 2022) to estimate the Wang GO semantic similarity matrix between groups of GO terms using the Best-Match Average (BMA) method. Semantic similarity (simBMA) between 2 groups (g1 and g2) is calculated as follows:

$$sim_{BMA}(g1, g2) = \frac{\sum_{l=i}^{m} max_{1 \leq j \leq m} sim(go1i, go2j) + \sum_{l=j}^{m} max_{1 \leq j \leq m} sim(go1i, go2j)}{m+n}$$

where m and n are the number of GO terms annotated in g1 and g2, respectively; and go1i and go2j are the GO term in position i (from 1 to m) from the g1 and the GO term in position j (from 1 to n) from the g2, respectively. simBMASemantic similarity values range from 0 to 1, with 0 meaning no similarity and 1 meaning (almost) identical.

We calculated the functional similarity between different groups (in this case, we compared the functional similarity between (1) enriched GO terms for gained and lost orthogroups at independent terrestrialisation events, (2) species using the hub genes involved in the response to a stress condition in each species, and (3) OGs containing hub genes in the response to each stress condition).

These distance matrices were subsequently clustered in constellatoR using the Affinity Propagation cluster algorithm to identify groups of genes exhibiting high functional similarity, effectively delineating functional clusters, as previously described[19,40]. To visualize these results, we used scatter plots where the functional clusters are represented as polygons.

The second strategy involved identifying metabolic pathways relevant for the response to each stress in each species. To achieve this, we assigned KEGG pathways using eggNOG-mapper v2.1.12[213] to each hub gene involved in the respective stress responses. Pathways categorised under 'Human Diseases' and 'Drug Development' in KEGG were excluded from further analysis. To account for differences in the number of hub genes identified per species, a pathway was considered relevant to the response if it comprised at least 1% of the total hub genes for that specific species-stress context. Functional convergence was then inferred by comparing the sets of metabolic pathways relevant to the response across different species and stress conditions.

Machine learning to identify habitat-predictive gene families

To identify orthogroups that may have been parallely expanded, contracted, gained, or lost in terrestrial lineages, we trained a machine learning XGBoost algorithm. We used as input the Species-OGs counts table provided by SonicParanoid2 v2.0.3a5 (outgroups removed), where we used OGs as predictive features, and the habitat of each species as the target variable. To reduce the number of features to use in the training, we pre-filtered the table to remove groups of OGs that would not be informative to predict habitat: (1) species-specific multi-copy genes, (2) OGs exclusive from fully-aquatic phyla (e.g., Porifera or Priapulida). From a total of 514,979 OGs, we ended up with 443,457 OGs after both filters.

We evaluated the performance of the model using a K-fold stratified cross-validation. Stratification (Fig. S290a) was performed based on “phylum” (Fig. S290b) and habitat (Fig. S290c) to account for sampling biases in the splitting of training and test sets due to overrepresentation of specific clades or habitats in our dataset (“effect of the phylogeny”). For “phylum”, given that there were not enough species per phylum for the 5-fold cross-validation, we stratified based on the phyla that contain terrestrial and aquatic species, and for the rest, we grouped phyla into higher categories (i.e., no-Bilateria, Xenacoelomorpha, Deuterostomia, Ecdysozoa, and Lophotrochozoa).

As the number of features greatly exceeded the number of training examples in the dataset, even after pre-filtering uninformative OGs, we applied dynamic recursive feature elimination (dRFE) to iteratively reduce dimensionality based on feature importance. We used a modified implementation of Python functions from dRFEtools[214], incorporating a strategy that combines feature importances and model accuracies across folds, as described in the original algorithm [215].

In brief, the method begins by training the model on all features across 5 cross-validation folds. For each fold, features are ranked according to their importance in the model. These rankings are then aggregated across folds, weighted by the classification accuracy of each fold (see below), to produce an overall feature score. All features with an importance of 0 are removed in the first iteration. Then, for subsequent iterations, the bottom 30% of features—those with the lowest aggregated scores—are removed, and the process repeats with the remaining features. This continues until only one feature remains (Fig. S290d).

The ranking criterion of feature i-th is computed as follows[215]:

$$F_i^{rank} = \sum_{k=1}^{n} F_{i,j} \times \frac{(A_j^{learn} + A_j^{validation})}{|A_j^{learn} - A_j^{validation}| + \varepsilon}$$

where j=1,.., n is the number of cross-validation folds, $F_{i,j}$, A_j^{learn} and $A_j^{validation}$ are the feature importance, the learning accuracy, and the validation accuracy of j-th feature, respectively. ε is a real number with a very small value.

From all the iterations of the dRFE, we identified the minimum number of features needed to accurately predict the environment on our species (top 130 OGs) by checking the number of features used that maximised validation accuracy and minimised log-loss in the test set (Fig. 6b,c).

To characterize those top 130 OGs (Table S69), we performed BLASTp against the nr database, and used PANGEA[216] to do a KEGG and REACTOME pathway enrichment against *D. melanogaster, D. rerio,* and *M. musculus* references (using as input genes from those species

contained in the top 130 OGs). For those OGs where there were no informative hits in any analyses, we checked the GO terms predicted by FANTASIA.

References

1. Selden, P. A. *Terrestrialization (Precambrian-Devonian) [Internet]*. *eLS*. (2005).
2. Vecoli, M., Clément, G. & Meyer-Berthaud, B. *The Terrestrialization Process: Modelling Complex Interactions at the Biosphere-Geosphere Interface*. (Geological Society of London, 2010).
3. Janvier, P. Terrestrialization: the early emergence of the concept. *Geol. Soc. Spec. Publ.* **339**, 5–9 (2010).
4. Garwood, R. J. & Edgecombe, G. D. Early terrestrial animals, evolution, and uncertainty. *Evolution (N. Y.)* **4**, 489–501 (2011).
5. Benton, M. J. Biodiversity on land and in the sea. *Geological Journal* **36**, 211–230 (2001).
6. Daley, A. C., Antcliffe, J. B., Drage, H. B. & Pates, S. Early fossil record of Euarthropoda and the Cambrian Explosion. *Proc Natl Acad Sci U S A* **115**, 5323–5331 (2018).
7. Buatois, L. A. *et al.* The Invasion of the Land in Deep Time: Integrating Paleozoic Records of Paleobiology, Ichnology, Sedimentology, and Geomorphology. *Integr Comp Biol* **62**, 297–331 (2022).
8. Cloudsley-Thompson, J. L. *Evolution and Adaptation of Terrestrial Arthropods*. (Springer Science & Business Media, 2012).
9. de Vries, J. & Archibald, J. M. Plant evolution: landmarks on the path to terrestrial life. *New Phytol* **217**, 1428–1434 (2018).
10. Dunlop, J. A., Scholtz, G. & Selden, P. A. Water-to-Land Transitions. *Arthropod Biology and Evolution* 417–439 (2013).

11. Evolutionary terrestrialization scenarios for soil invertebrates. *Pedobiologia* **87-88**, 150753 (2021).
12. Evolutionary terrestrialization scenarios for soil invertebrates. *Pedobiologia* **87-88**, 150753 (2021).
13. Allen, K. & Briggs, D. E. G. *Evolution and the Fossil Record*. (1989).
14. Long, J. A. & Gordon, M. S. The Greatest Step in Vertebrate History: A Paleobiological Review of the Fish-Tetrapod Transition*. *Physiological and Biochemical Zoology* (2004) doi:10.1086/425183.
15. Benton, M. J. *Cowen's History of Life*. (John Wiley & Sons, 2019).
16. Minter, N. J. *et al.* The Prelude to Continental Invasion. *The Trace-Fossil Record of Major Evolutionary Events* 157–204 (2016).
17. Wang, K. *et al.* African lungfish genome sheds light on the vertebrate water-to-land transition. *Cell* **184**, 1362–1376.e18 (2021).
18. Meyer, A. *et al.* Giant lungfish genome elucidates the conquest of land by vertebrates. *Nature* **590**, 284–289 (2021).
19. Aristide, L. & Fernández, R. Genomic insights into mollusk terrestrialization: Parallel and convergent gene family expansions as key facilitators in out-of-the-sea transitions. *Genome Biol. Evol.* **15**, (2023).
20. Benítez-Álvarez, L. *et al.* Genomic exaptation and regulatory landscape shifts as key mechanisms enabling flatworm terrestrialization. *bioRxiv* 2025.01.09.632089 (2025) doi:10.1101/2025.01.09.632089.
21. Schartl, M. *et al.* The genomes of all lungfish inform on genome expansion and tetrapod evolution. *Nature* **634**, 96–103 (2024).
22. Bi, X. *et al.* Tracing the genetic footprints of vertebrate landing in non-teleost ray-finned fishes. *Cell* **184**, 1377–1391.e14 (2021).

23. Martínez-Redondo, G. I. *et al.* Parallel duplication and loss of aquaporin-coding genes during the 'out of the sea' transition as potential key drivers of animal terrestrialization. *Mol. Ecol.* **32**, 2022–2040 (2023).

24. Fleming, J. F., Pisani, D. & Arakawa, K. The Evolution of Temperature and Desiccation-Related Protein Families in Tardigrada Reveals a Complex Acquisition of Extremotolerance. *Genome Biol Evol* **16**, (2024).

25. Fernández, R. & Gabaldón, T. Gene gain and loss across the metazoan tree of life. *Nat. Ecol. Evol.* **4**, 524–533 (2020).

26. Richter, D. J., Fozouni, P., Eisen, M. B. & King, N. Gene family innovation, conservation and loss on the animal stem lineage. *Elife* **7**, e34226 (2018).

27. Domazet-Lošo, M., Široki, T., Šimičević, K. & Domazet-Lošo, T. Macroevolutionary dynamics of gene family gain and loss along multicellular eukaryotic lineages. *Nature Communications* **15**, 1–22 (2024).

28. Wolf, Y. I. & Koonin, E. V. Genome reduction as the dominant mode of evolution. *BioEssays* **35**, 829–837 (2013).

29. Dadras, A. *et al.* Environmental gradients reveal stress hubs pre-dating plant terrestrialization. *Nat. Plants* **9**, 1419–1438 (2023).

30. Zhu, C. *et al.* WGCNA based identification of hub genes associated with cold response and development in Apis mellifera metamorphic pupae. *Front. Physiol.* **14**, 1169301 (2023).

31. Razalli, I. I. *et al.* Identification and validation of hub genes associated with biotic and abiotic stresses by modular gene co-expression analysis in Oryza sativa L. *Sci. Rep.* **15**, 8465 (2025).

32. William J. Lennarz and M. Daniel Lane. Rab Family. in *Encyclopedia of Biological Chemistry (Second Edition)* (ed. William J. Lennarz and M. Daniel Lane) 1–6

(Academic Press, 2013).

33. Hirosawa-Takamori, M., Chung, H. & Jäckle, H. Conserved selenoprotein synthesis is not critical for oxidative stress defence and the lifespan of Drosophila. *EMBO reports* (2004) doi:10.1038/sj.embor.7400097.

34. Gao, M. *et al.* The deubiquitinase USP7 regulates oxidative stress through stabilization of HO-1. *Oncogene* **41**, 4018–4027 (2022).

35. Jiang, W. I. *et al.* Early-life stress triggers long-lasting organismal resilience and longevity via tetraspanin. *Science Advances* (2024) doi:10.1126/sciadv.adj3880.

36. Mani, B., Agarwal, M. & Katiyar-Agarwal, S. Comprehensive Expression Profiling of Rice Tetraspanin Genes Reveals Diverse Roles During Development and Abiotic Stress. *Front. Plant Sci.* **6**, 165506 (2015).

37. Thomas E Ceremuga and Xiang-Lan Yao and Yang Xia and Dhritiman Mukherjee and Joseph T McCabe. Osmotic stress increases cullin-5 (cul-5) mRNA in the rat cerebral cortex, hypothalamus and kidney. *Neuroscience Research* **45**, 305–311 (2003).

38. Karachitos, A., Grabiński, W., Baranek, M. & Kmita, H. Redox-Sensitive VDAC: A Possible Function as an Environmental Stress Sensor Revealed by Bioinformatic Analysis. *Front. Physiol.* **12**, 750627 (2021).

39. Bohutínská, M. & Peichel, C. L. Divergence time shapes gene reuse during repeated adaptation. *Trends Ecol Evol* **39**, 396–407 (2024).

40. Balart-García, P. *et al.* Parallel and convergent genomic changes underlie independent subterranean colonization across beetles. *Nat. Commun.* **14**, 3842 (2023).

41. Ishikawa, A., Yamanouchi, S., Iwasaki, W. & Kitano, J. Convergent copy number increase of genes associated with freshwater colonization in fishes. *Philos. Trans. R. Soc. Lond. B Biol. Sci.* **377**, 20200509 (2022).

42. Davín, A. A. *et al.* A geological timescale for bacterial evolution and oxygen adaptation.

Science **388**, eadp1853 (2025).

43. Gonçalves, C. *et al.* Diverse signatures of convergent evolution in cactus-associated yeasts. *PLOS Biology* **22**, e3002832 (2024).

44. Brand, P. *et al.* The origin of the odorant receptor gene family in insects. *Elife* **7**, e38340 (2018).

45. Werck-Reichhart, D., Nelson, D. R. & Renault, H. Cytochromes P450 evolution in the plant terrestrialization context. *Philos. Trans. R. Soc. Lond. B Biol. Sci.* **379**, 20230363 (2024).

46. Loo, R. L., Chan, Q., Nicholson, J. K. & Holmes, E. Balancing the equation: A natural history of trimethylamine and trimethylamine-N-oxide. *J. Proteome Res.* **21**, 560–589 (2022).

47. Padilla, S., Prado, R. & Anitua, E. An evolutionary history of F12 gene: Emergence, loss, and vulnerability with the environment as a driver. *Bioessays* **45**, e2300077 (2023).

48. Green, J., Taylor, J. J., Hindes, A., Johnson, S. L. & Goldsmith, M. I. A gain of function mutation causing skeletal overgrowth in the rapunzel mutant. *Dev. Biol.* **334**, 224–234 (2009).

49. Lobanov, A. V., Hatfield, D. L. & Gladyshev, V. N. Eukaryotic selenoproteins and selenoproteomes. *Biochim. Biophys. Acta* **1790**, 1424–1428 (2009).

50. Lobanov, A. V. *et al.* Evolutionary dynamics of eukaryotic selenoproteomes: large selenoproteomes may associate with aquatic life and small with terrestrial life. *Genome Biol.* **8**, R198 (2007).

51. Doughty, T. W. *et al.* Stress-induced expression is enriched for evolutionarily young genes in diverse budding yeasts. *Nature Communications* **11**, 1–9 (2020).

52. Xie, K. T. *et al.* DNA fragility in the parallel evolution of pelvic reduction in stickleback fish. *Science* (2019) doi:10.1126/science.aan1425.

53. Jacob, F. Evolution and Tinkering. *Science* (1977) doi:10.1126/science.860134.

54. Watson-Zink, V. M., Grosberg, R. K., Lai, J. C. Y. & Bay, R. A. Transcriptomic responses of gecarcinid land crabs to acute and prolonged desiccation stress. *bioRxiv* 2024.07.03.601969 (2024) doi:10.1101/2024.07.03.601969.

55. Dong, Y., Krishnamoorthi, S., Tan, G. Z. H., Poh, Z. Y. & Urano, D. Co-option of plant gene regulatory network in nutrient responses during terrestrialization. *Nature Plants* **10**, 1955–1968 (2024).

56. Helsen, J. *et al.* Gene Loss Predictably Drives Evolutionary Adaptation. *Mol Biol Evol* **37**, 2989–3002 (2020).

57. Albalat, R. & Cañestro, C. Evolution by gene loss. *Nat. Rev. Genet.* **17**, 379–391 (2016).

58. Xia, S., Chen, J., Arsala, D., Emerson, J. J. & Long, M. Functional innovation through new genes as a general evolutionary process. *Nature Genetics* **57**, 295–309 (2025).

59. Martínez-Redondo, G. I. *et al.* MATEdb2, a collection of high-quality metazoan proteomes across the animal tree of life to speed up phylogenomic studies. *Genome Biol. Evol.* **16**, evae235 (2024).

60. Huerta-Cepas, J., Serra, F. & Bork, P. ETE 3: Reconstruction, analysis, and visualization of phylogenomic data. *Mol. Biol. Evol.* **33**, 1635–1638 (2016).

61. Ocaña-Pallarès, E. *et al.* Divergent genomic trajectories predate the origin of animals and fungi. *Nature* **609**, 747–753 (2022).

62. Laumer, C. E. *et al.* Revisiting metazoan phylogeny with genomic sampling of all phyla. *Proc. Biol. Sci.* **286**, 20190831 (2019).

63. Kenny, N. J. *et al.* Tracing animal genomic evolution with the chromosomal-level assembly of the freshwater sponge Ephydatia muelleri. *Nature Communications* **11**, 1–11 (2020).

64. Plese, B. *et al.* Mitochondrial evolution in the Demospongiae (Porifera): Phylogeny,

divergence time, and genome biology. *Molecular Phylogenetics and Evolution* **155**, 107011 (2021).

65. Simion, P. *et al.* A Large and Consistent Phylogenomic Dataset Supports Sponges as the Sister Group to All Other Animals. *Current Biology* **27**, 958–967 (2017).

66. DeBiasse, M. B. *et al.* A Cnidarian Phylogenomic Tree Fitted With Hundreds of 18S Leaves. *BSSB* **3**, (2024).

67. Kayal, E. *et al.* Phylogenomics provides a robust topology of the major cnidarian lineages and insights on the origins of key organismal traits. *BMC Evolutionary Biology* **18**, 1–18 (2018).

68. Atherton, S. & Jondelius, U. Phylogenetic assessment and systematic revision of the acoel family Isodiametridae. *Zool J Linn Soc* **194**, 736–760 (2021).

69. Reich, A., Dunn, C., Akasaka, K. & Wessel, G. Phylogenomic analyses of Echinodermata support the sister groups of Asterozoa and Echinozoa. *PLoS One* **10**, e0119627 (2015).

70. Cannon, J. T. *et al.* Phylogenomic Resolution of the Hemichordate and Echinoderm Clade. *Current Biology* **24**, 2827–2832 (2014).

71. Zhang, Q.-L. *et al.* A Phylogenomic Framework and Divergence History of Cephalochordata Amphioxus. *Front Physiol* **9**, 1833 (2018).

72. Irisarri, I. *et al.* Phylotranscriptomic consolidation of the jawed vertebrate timetree. *Nature Ecology & Evolution* **1**, 1370–1378 (2017).

73. Yu, D. *et al.* Hagfish genome elucidates vertebrate whole-genome duplication events and their evolutionary consequences. *Nature Ecology & Evolution* **8**, 519–535 (2024).

74. Hughes, L. C. *et al.* Comprehensive phylogeny of ray-finned fishes (Actinopterygii) based on transcriptomic and genomic data. *Proc Natl Acad Sci U S A* **115**, 6249–6254 (2018).

75. Bian, C. *et al.* Divergence, evolution and adaptation in ray-finned fish genomes. *Science China Life Sciences* **62**, 1003–1018 (2019).

76. Parey, E. *et al.* Genome structures resolve the early diversification of teleost fishes. *Science* **379**, 572–575 (2023).

77. Hime, P. M. *et al.* Phylogenomics Reveals Ancient Gene Tree Discordance in the Amphibian Tree of Life. *Syst Biol* **70**, 49–66 (2020).

78. Giribet, G. & Edgecombe, G. D. Current Understanding of Ecdysozoa and its Internal Phylogenetic Relationships. *Integr Comp Biol* **57**, 455–466 (2017).

79. Giacomelli, M. *et al.* CAT-Posterior Mean Site Frequencies Improves Phylogenetic Modeling Under Maximum Likelihood and Resolves Tardigrada as the Sister of Arthropoda Plus Onychophora. *Genome Biol Evol* **17**, evae273 (2024).

80. Herranz, M., Stiller, J., Worsaae, K. & Sørensen, M. V. Phylogenomic analyses of mud dragons (Kinorhyncha). *Molecular Phylogenetics and Evolution* **168**, 107375 (2022).

81. Ahmed, M. *et al.* Phylogenomic Analysis of the Phylum Nematoda: Conflicts and Congruences With Morphology, 18S rRNA, and Mitogenomes. *Front. Ecol. Evol.* **9**, (2022).

82. Bhat, A. H. *et al.* Morphological, Morphometrical and Molecular Characterization of Oscheius siddiqii Tabassum and Shahina, 2010 (Rhabditida, Rhabditidae) from India with Its Taxonomic Consequences for the Subgenus Oscheius Andrássy, 1976. *Biology* **10**, 1239 (2021).

83. Abolafia, J. & Vecchi, M. Redescription and phylogenetic analysis of the type species of the genus Thorne, 1938 (Rhabditida, Panagrolaimidae), Thorne, 1938, including the first SEM study. *J Nematol* **53**, (2021).

84. Bleidorn, C., Schmidt-Rhaesa, A. & Garey, J. R. Systematic relationships of Nematomorpha based on molecular and morphological data. *Invertebrate Biology* **121**,

357–364 (2002).

85. Fleming, J. F. & Arakawa, K. Systematics of tardigrada: A reanalysis of tardigrade taxonomy with specific reference to Guil et al. (2019). *Zoologica Scripta* **50**, 376–382 (2021).

86. Guil, N. & Giribet, G. A comprehensive molecular phylogeny of tardigrades-adding genes and taxa to a poorly resolved phylum-level phylogeny. *Cladistics* **28**, 21–49 (2012).

87. Guil, N., Jørgensen, A. & Kristensen, R. An upgraded comprehensive multilocus phylogeny of the Tardigrada tree of life. *Zoologica Scripta* **48**, 120–137 (2019).

88. Nichols, P. B., Nelson, D. R. & Garey, J. R. A Family Level Analysis of Tardigrade Phylogeny. *Hydrobiologia* **558**, 53–60 (2006).

89. Stec, D., Vecchi, M., Calhim, S. & Michalczyk, Ł. New multilocus phylogeny reorganises the family Macrobiotidae (Eutardigrada) and unveils complex morphological evolution of the Macrobiotus hufelandi group. *Molecular Phylogenetics and Evolution* **160**, 106987 (2021).

90. Stec, D., Vecchi, M., Maciejowski, W. & Michalczyk, Ł. Resolving the systematics of Richtersiidae by multilocus phylogeny and an integrative redescription of the nominal species for the genus Crenubiotus (Tardigrada). *Scientific Reports* **10**, 1–20 (2020).

91. Baker, C. M., Buckman-Young, R. S., Costa, C. S. & Giribet, G. Phylogenomic Analysis of Velvet Worms (Onychophora) Uncovers an Evolutionary Radiation in the Neotropics. *Mol Biol Evol* **38**, 5391–5404 (2021).

92. Costa, C. S., Giribet FLS, G. & Pinto-Da-Rocha, R. Morphological and molecular phylogeny of Epiperipatus (Onychophora: Peripatidae): a combined approach. *Zool J Linn Soc* **192**, 763–793 (2020).

93. Giribet, G. & Edgecombe, G. D. The Phylogeny and Evolutionary History of

Arthropods. *Current Biology* **29**, R592–R602 (2019).

94. Ballesteros, J. A. *et al.* Comprehensive Species Sampling and Sophisticated Algorithmic Approaches Refute the Monophyly of Arachnida. *Mol Biol Evol* **39**, msac021 (2022).

95. Xiong, Q. *et al.* Comparative Genomics Reveals Insights into the Divergent Evolution of Astigmatic Mites and Household Pest Adaptations. *Mol Biol Evol* **39**, msac097 (2022).

96. Pepato, A. R., Costa, S. G. dos S., Harvey, M. S. & Klimov, P. B. One-way ticket to the blue: A large-scale, dated phylogeny revealed asymmetric land-to-water transitions in acariform mites (Acari: Acariformes). *Molecular Phylogenetics and Evolution* **177**, 107626 (2022).

97. Ontano, A. Z. *et al.* Taxonomic Sampling and Rare Genomic Changes Overcome Long-Branch Attraction in the Phylogenetic Placement of Pseudoscorpions. *Mol Biol Evol* **38**, 2446–2467 (2021).

98. Kallal, R. J. *et al.* Converging on the orb: denser taxon sampling elucidates spider phylogeny and new analytical methods support repeated evolution of the orb web. *Cladistics* **37**, 298–316 (2021).

99. Wang, J., Bai, Y., Zhao, H., Mu, R. & Dong, Y. Reinvestigating the phylogeny of Myriapoda with more extensive taxon sampling and novel genetic perspective. *PeerJ* **9**, e12691 (2021).

100. Giribet, G. & Edgecombe, G. D. Conflict between datasets and phylogeny of centipedes: an analysis based on seven genes and morphology. *Proceedings of the Royal Society B: Biological Sciences* (2005) doi:10.1098/rspb.2005.3365.

101. Giribet, G. & Edgecombe, G. D. Stable phylogenetic patterns in scutigeromorph centipedes (Myriapoda : Chilopoda : Scutigeromorpha): dating the diversification of an ancient lineage of terrestrial arthropods. *Invert. Systematics* **27**, 485–501 (2013).

102. Bernot, J. P. *et al.* Major Revisions in Pancrustacean Phylogeny and Evidence of

Sensitivity to Taxon Sampling. *Mol Biol Evol* **40**, msad175 (2023).

103. Schwentner, M., Richter, S., Christopher Rogers, D. & Giribet, G. Tetraconatan phylogeny with special focus on Malacostraca and Branchiopoda: highlighting the strength of taxon-specific matrices in phylogenomics. *Proceedings of the Royal Society B* doi:10.1098/rspb.2018.1524.

104. Oakley, T. H., Wolfe, J. M., Lindgren, A. R. & Zaharoff, A. K. Phylotranscriptomics to Bring the Understudied into the Fold: Monophyletic Ostracoda, Fossil Placement, and Pancrustacean Phylogeny. *Mol Biol Evol* **30**, 215–233 (2012).

105. Hiruta, S. F., Kobayashi, N., Katoh, T. & Kajihara, H. Molecular Phylogeny of Cypridoid Freshwater Ostracods (Crustacea: Ostracoda), Inferred from 18S and 28S rDNA Sequences. *jzoo* **33**, 179–185 (2016).

106. Luchetti, A. *et al.* Comparative genomics of tadpole shrimps (Crustacea, Branchiopoda, Notostraca): Dynamic genome evolution against the backdrop of morphological stasis. *Genomics* **113**, 4163–4172 (2021).

107. Mathers, T. C. *et al.* High lability of sexual system over 250 million years of evolution in morphologically conservative tadpole shrimps. *BMC Evolutionary Biology* **13**, 1–12 (2013).

108. Copilaş-Ciocianu, D., Borko, Š. & Fišer, C. The late blooming amphipods: Global change promoted post-Jurassic ecological radiation despite Palaeozoic origin. *Molecular Phylogenetics and Evolution* **143**, 106664 (2020).

109. Li, J.-Y., Zeng, C., Yan, G.-Y. & He, L.-S. Characterization of the mitochondrial genome of an ancient amphipod Halice sp. MT-2017 (Pardaliscidae) from 10,908 m in the Mariana Trench. *Scientific Reports* **9**, 1–15 (2019).

110. Drumm, D. T. Phylogenetic Relationships of Tanaidacea (Eumalacostraca: Peracarida) Inferred from Three Molecular Loci. *J Crustacean Biol* **30**, 692–698 (2010).

111. Dimitriou, A. C., Taiti, S. & Sfenthourakis, S. Genetic evidence against monophyly of Oniscidea implies a need to revise scenarios for the origin of terrestrial isopods. *Scientific Reports* **9**, 1–10 (2019).

112. Lins, L. S. F., Ho, S. Y. W. & Lo, N. An evolutionary timescale for terrestrial isopods and a lack of molecular support for the monophyly of Oniscidea (Crustacea: Isopoda). *Organisms Diversity & Evolution* **17**, 813–820 (2017).

113. Wägele, J.-W., Holland, B., Dreyer, H. & Hackethal, B. Searching factors causing implausible non-monophyly: ssu rDNA phylogeny of Isopoda Asellota (Crustacea: Peracarida) and faster evolution in marine than in freshwater habitats. *Molecular Phylogenetics and Evolution* **28**, 536–551 (2003).

114. Javidkar, M., Cooper, S. J. B., King, R. A., Humphreys, W. F. & Austin, A. D. Molecular phylogenetic analyses reveal a new southern hemisphere oniscidean family (Crustacea : Isopoda) with a unique water transport system. *Invert. Systematics* **29**, 554–577 (2015).

115. Vereshchaka, A. L., Kulagin, D. N. & Lunina, A. A. A phylogenetic study of krill (Crustacea: Euphausiacea) reveals new taxa and co-evolution of morphological characters. *Cladistics* **35**, 150–172 (2019).

116. Wolfe, J. M. *et al.* A phylogenomic framework, evolutionary timeline and genomic resources for comparative studies of decapod crustaceans. *Proceedings of the Royal Society B* (2019) doi:10.1098/rspb.2019.0079.

117. Chak, S. T. C., Barden, P. & Baeza, J. A. The complete mitochondrial genome of the eusocial sponge-dwelling snapping shrimp Synalpheus microneptunus. *Scientific Reports* **10**, 1–10 (2020).

118. Vereshchaka, A. L. The shrimp superfamily Sergestoidea: a global phylogeny with definition of new families and an assessment of the pathways into principal biotopes.

Royal Society Open Science (2017) doi:10.1098/rsos.170221.

119. Bracken-Grissom, H. D. *et al.* A comprehensive and integrative reconstruction of evolutionary history for Anomura (Crustacea: Decapoda). *BMC Evolutionary Biology* **13**, 1–29 (2013).

120. Wolfe, J. M. *et al.* Convergent Adaptation of True Crabs (Decapoda: Brachyura) to a Gradient of Terrestrial Environments. *Syst Biol* **73**, 247–262 (2023).

121. Tsang, C. T. T., Schubart, C., Chu, K. H., Ng, P. K. L. & Tsang, L. M. Molecular phylogeny of Thoracotremata crabs (Decapoda, Brachyura): Toward adopting monophyletic superfamilies, invasion history into terrestrial habitats and multiple origins of symbiosis. *Molecular Phylogenetics and Evolution* **177**, 107596 (2022).

122. Misof, B. *et al.* Phylogenomics resolves the timing and pattern of insect evolution. *Science* (2014) doi:10.1126/science.1257570.

123. Sun, X. *et al.* Phylomitogenomic analyses on collembolan higher taxa with enhanced taxon sampling and discussion on method selection. *PLOS ONE* **15**, e0230827 (2020).

124. Yu, D. *et al.* Phylogenomics of Elongate-Bodied Springtails Reveals Independent Transitions from Aboveground to Belowground Habitats in Deep Time. *Syst Biol* **71**, 1023–1031 (2022).

125. Yu, D. *et al.* Molecular phylogeny and trait evolution in an ancient terrestrial arthropod lineage: Systematic revision and implications for ecological divergence (Collembola, Tomocerinae). *Molecular Phylogenetics and Evolution* **154**, 106995 (2021).

126. Sendra, A., Jiménez-Valverde, A., Selfa, J. & Reboleira, A. S. P. Diversity, ecology, distribution and biogeography of Diplura. *Insect Conservation and Diversity* **14**, 415–425 (2021).

127. Carapelli, A. *et al.* Going Deeper into High and Low Phylogenetic Relationships of Protura. *Genes* **10**, 292 (2019).

128. Wang, Z., Shi, Y., Qiu, Z., Che, Y. & Lo, N. Reconstructing the phylogeny of Blattodea: robust support for interfamilial relationships and major clades. *Scientific Reports* **7**, 1–8 (2017).

129. Johnson, K. P. *et al.* Phylogenomics and the evolution of hemipteroid insects. *Proceedings of the National Academy of Sciences* **115**, 12775–12780 (2018).

130. McKenna, D. D. *et al.* The evolution and genomic basis of beetle diversity. *Proceedings of the National Academy of Sciences* **116**, 24729–24737 (2019).

131. Kawahara, A. Y. *et al.* Phylogenomics reveals the evolutionary timing and pattern of butterflies and moths. *Proceedings of the National Academy of Sciences* **116**, 22657–22663 (2019).

132. Peters, R. S. *et al.* Evolutionary History of the Hymenoptera. *Current Biology* **27**, 1013–1018 (2017).

133. Wiegmann, B. M. *et al.* Episodic radiations in the fly tree of life. *Proceedings of the National Academy of Sciences* **108**, 5690–5695 (2011).

134. Khalturin, K. *et al.* Polyzoa is back: The effect of complete gene sets on the placement of Ectoprocta and Entoprocta. *Sci Adv* **8**, eabo4400 (2022).

135. Lu, T.-M., Kanda, M., Satoh, N. & Furuya, H. The phylogenetic position of dicyemid mesozoans offers insights into spiralian evolution. *Zoological Lett* **3**, 6 (2017).

136. Marlétaz, F., Peijnenburg, K. T. C. A., Goto, T., Satoh, N. & Rokhsar, D. S. A New Spiralian Phylogeny Places the Enigmatic Arrow Worms among Gnathiferans. *Current Biology* **29**, 312–318.e3 (2019).

137. Gasmi, S. *et al.* Evolutionary history of Chaetognatha inferred from molecular and morphological data: a case study for body plan simplification. *Frontiers in Zoology* **11**, 1–25 (2014).

138. Melone, G., Ricci, C., Segers, H. & Wallace, R. L. Phylogenetic relationships of phylum

Rotifera with emphasis on the families of Bdelloidea. *Hydrobiologia* **387**, 101–107 (1998).

139. Benítez-Álvarez, L. *et al.* Disentangling the evolutionary history of terrestrial planarians through phylogenomics. *bioRxiv* 2025.01.07.631701 (2025) doi:10.1101/2025.01.07.631701.

140. Laumer, C. E., Hejnol, A. & Giribet, G. Nuclear genomic signals of the 'microturbellarian' roots of platyhelminth evolutionary innovation. (2015) doi:10.7554/eLife.05503.

141. Orr, R. J. S. *et al.* Paleozoic origins of cheilostome bryozoans and their parental care inferred by a new genome-skimmed phylogeny. *Sci Adv* **8**, eabm7452 (2022).

142. Saadi, A. J. *et al.* Phylogenomics reveals deep relationships and diversification within phylactolaemate bryozoans. *Proceedings of the Royal Society B* (2022) doi:10.1098/rspb.2022.1504.

143. Fuchs, J., Iseto, T., Hirose, M., Sundberg, P. & Obst, M. The first internal molecular phylogeny of the animal phylum Entoprocta (Kamptozoa). *Mol Phylogenet Evol* **56**, 370–379 (2010).

144. Chen, Z. *et al.* A genome-based phylogeny for Mollusca is concordant with fossils and morphology. *Science* (2025) doi:10.1126/science.ads0215.

145. Song, H. *et al.* Scaphopoda is the sister taxon to Bivalvia: Evidence of ancient incomplete lineage sorting. *Proceedings of the National Academy of Sciences* **120**, e2302361120 (2023).

146. Irisarri, I., Uribe, J. E., Eernisse, D. J. & Zardoya, R. A mitogenomic phylogeny of chitons (Mollusca: Polyplacophora). *BMC Evolutionary Biology* **20**, 1–15 (2020).

147. Kocot, K. M., Todt, C., Mikkelsen, N. T. & Halanych, K. M. Phylogenomics of Aplacophora (Mollusca, Aculifera) and a solenogaster without a foot. *Proceedings of the*

Royal Society B (2019) doi:10.1098/rspb.2019.0115.

148. Anderson, F. E. & Lindgren, A. R. Phylogenomic analyses recover a clade of large-bodied decapodiform cephalopods. *Molecular Phylogenetics and Evolution* **156**, 107038 (2021).

149. Lindgren, A. R. Molecular inference of phylogenetic relationships among Decapodiformes (Mollusca: Cephalopoda) with special focus on the squid Order Oegopsida. *Molecular Phylogenetics and Evolution* **56**, 77–90 (2010).

150. Uribe, J. E. & Zardoya, R. Revisiting the phylogeny of Cephalopoda using complete mitochondrial genomes. *J Molluscan Stud* **83**, 133–144 (2017).

151. Uribe, J. E. *et al.* A Phylogenomic Backbone for Gastropod Molluscs. *Syst Biol* **71**, 1271–1280 (2022).

152. Zhong, Z. *et al.* New mitogenomes in deep-water endemic Cocculinida and Neomphalida shed light on lineage-specific gene orders in major gastropod clades. *Front. Ecol. Evol.* **10**, 973485 (2022).

153. Cunha, T. J., Reimer, J. D. & Giribet, G. Investigating Sources of Conflict in Deep Phylogenomics of Vetigastropod Snails. *Syst Biol* **71**, 1009–1022 (2021).

154. Xu, T., Qi, L., Kong, L. & Li, Q. Mitogenomics reveals phylogenetic relationships of Patellogastropoda (Mollusca, Gastropoda) and dynamic gene rearrangements. *Zoologica Scripta* **51**, 147–160 (2022).

155. Cunha, T. J. & Giribet, G. A congruent topology for deep gastropod relationships. *Proceedings of the Royal Society B* (2019) doi:10.1098/rspb.2018.2776.

156. Uribe, J. E., Colgan, D., Castro, L. R., Kano, Y. & Zardoya, R. Phylogenetic relationships among superfamilies of Neritimorpha (Mollusca: Gastropoda). *Molecular Phylogenetics and Evolution* **104**, 21–31 (2016).

157. Yang, H. *et al.* Comparative Characterization of the Complete Mitochondrial Genomes

of the Three Apple Snails (Gastropoda: Ampullariidae) and the Phylogenetic Analyses. *International Journal of Molecular Sciences* **19**, 3646 (2018).

158. Colgan, D. J., Ponder, W. F., Beacham, E. & Macaranas, J. Molecular phylogenetics of Caenogastropoda (Gastropoda: Mollusca). *Molecular Phylogenetics and Evolution* **42**, 717–737 (2007).

159. Goodheart, J. A. & Wägele, H. Phylogenomic analysis and morphological data suggest left-right swimming behavior evolved prior to the origin of the pelagic Phylliroidae (Gastropoda: Nudibranchia). *Organisms Diversity & Evolution* **20**, 657–667 (2020).

160. Krug, P. J. *et al.* Phylogenomic resolution of the root of Panpulmonata, a hyperdiverse radiation of gastropods: new insight into the evolution of air breathing. *Proceedings of the Royal Society B* (2022) doi:10.1098/rspb.2021.1855.

161. Razkin, O. *et al.* Molecular phylogeny of the western Palaearctic Helicoidea (Gastropoda, Stylommatophora). *Molecular Phylogenetics and Evolution* **83**, 99–117 (2015).

162. Doğan, Ö., Schrödl, M. & Chen, Z. The complete mitogenome of Arion vulgaris Moquin-Tandon, 1855 (Gastropoda: Stylommatophora): mitochondrial genome architecture, evolution and phylogenetic considerations within Stylommatophora. *PeerJ* **8**, e8603 (2020).

163. González, V. L. *et al.* A phylogenetic backbone for Bivalvia: an RNA-seq approach. *Proceedings of the Royal Society B: Biological Sciences* (2015) doi:10.1098/rspb.2014.2332.

164. Smith, C. H. A High-Quality Reference Genome for a Parasitic Bivalve with Doubly Uniparental Inheritance (Bivalvia: Unionida). *Genome Biol Evol* **13**, evab029 (2021).

165. Lemer, S., González, V. L., Bieler, R. & Giribet, G. Cementing mussels to oysters in the pteriomorphian tree: a phylogenomic approach. *Proceedings of the Royal Society B:*

Biological Sciences (2016) doi:10.1098/rspb.2016.0857.

166. Salvi, D. & Mariottini, P. Molecular taxonomy in 2D: a novel ITS2 rRNA sequence-structure approach guides the description of the oysters' subfamily Saccostreinae and the genus Magallana (Bivalvia: Ostreidae). *Zool J Linn Soc* **179**, 263–276 (2016).

167. Helm, C. *et al.* Convergent evolution of the ladder-like ventral nerve cord in Annelida. *Frontiers in Zoology* **15**, 1–17 (2018).

168. Li, Y. *et al.* Genomic adaptations to chemosymbiosis in the deep-sea seep-dwelling tubeworm Lamellibrachia luymesi. *BMC Biology* **17**, 1–14 (2019).

169. Xu, T. *et al.* The Morphology, Mitogenome, Phylogenetic Position, and Symbiotic Bacteria of a New Species of Sclerolinum (Annelida: Siboglinidae) in the South China Sea. *Front. Mar. Sci.* **8**, 793645 (2022).

170. Andrade, S. C. S. *et al.* Articulating 'Archiannelids': Phylogenomics and Annelid Relationships, with Emphasis on Meiofaunal Taxa. *Mol Biol Evol* **32**, 2860–2875 (2015).

171. Lemer, S. *et al.* Re-evaluating the phylogeny of Sipuncula through transcriptomics. *Molecular Phylogenetics and Evolution* **83**, 174–183 (2015).

172. Struck, T. H. *et al.* The Evolution of Annelids Reveals Two Adaptive Routes to the Interstitial Realm. *Current Biology* **25**, 1993–1999 (2015).

173. Tilic, E., Stiller, J., Campos, E., Pleijel, F. & Rouse, G. W. Phylogenomics resolves ambiguous relationships within Aciculata (Errantia, Annelida). *Molecular Phylogenetics and Evolution* **166**, 107339 (2022).

174. Martín-Durán, J. M. *et al.* Conservative route to genome compaction in a miniature annelid. *Nat. Ecol. Evol.* **5**, 231–242 (2021).

175. Tilic, E., Sayyari, E., Stiller, J., Mirarab, S. & Rouse, G. W. More is needed—Thousands of loci are required to elucidate the relationships of the 'flowers of the sea'

(Sabellida, Annelida). *Molecular Phylogenetics and Evolution* **151**, 106892 (2020).

176. Stiller, J., Tilic, E., Rousset, V., Pleijel, F. & Rouse, G. W. Spaghetti to a Tree: A Robust Phylogeny for Terebelliformia (Annelida) Based on Transcriptomes, Molecular and Morphological Data. *Biology* **9**, 73 (2020).

177. Erséus, C. *et al.* Phylogenomic analyses reveal a Palaeozoic radiation and support a freshwater origin for clitellate annelids. *Zool. Scr.* **49**, 614–640 (2020).

178. Tong, L. *et al.* The genome of medicinal leech (Whitmania pigra) and comparative genomic study for exploration of bioactive ingredients. *BMC Genomics* **23**, 1–13 (2022).

179. Andrade, S. C. S. *et al.* A Transcriptomic Approach to Ribbon Worm Systematics (Nemertea): Resolving the Pilidiophora Problem. *Mol Biol Evol* **31**, 3206–3215 (2014).

180. Chernyshev, A. V., Polyakova, N. E., Norenburg, J. L. & Kajihara, H. A molecular phylogeny of Tetrastemma and its allies (Nemertea, Monostilifera). *Zoologica Scripta* **50**, 824–836 (2021).

181. Chernyshev, A. V. & Polyakova, N. E. Distribution and Phylogenetic Position of the Antarctic Ribbon Worm Heteronemertes longifissa (Nemertea, Pilidiophora). *Water* **15**, 809 (2023).

182. Bapst, D. W., Schreiber, H. A. & Carlson, S. J. Combined Analysis of Extant Rhynchonellida (Brachiopoda) using Morphological and Molecular Data. *Syst Biol* **67**, 32–48 (2018).

183. Carlson, S. J. The evolution of brachiopoda. *Annu. Rev. Earth Planet. Sci.* **44**, 409–438 (2016).

184. Hirose, M., Fukiage, R., Katoh, T. & Kajihara, H. Description and molecular phylogeny of a new species of Phoronis (Phoronida) from Japan, with a redescription of topotypes of P. ijimai Oka, 1897. *Description and molecular phylogeny of a new species of Phoronis (Phoronida) from Japan, with a redescription of topotypes of P. ijimai Oka,*

1897 **398**, 1–31 (2014).

185. WoRMS - World Register of Marine Species. https://www.marinespecies.org/aphia.php?p=popup&name=citation.

186. Bapst, D. W. paleotree: an R package for paleontological and phylogenetic analyses of evolution. *Methods in Ecology and Evolution* **3**, 803–807 (2012).

187. Cosentino, S., Sriswasdi, S. & Iwasaki, W. SonicParanoid2: fast, accurate, and comprehensive orthology inference with machine learning and language models. *Genome Biol.* **25**, 195 (2024).

188. Martínez-Redondo, G. I. *et al.* Leveraging Natural Language Processing models to decode the dark proteome across the Animal Tree of Life. *Evolutionary Biology* (2024).

189. TopGO. *Bioconductor* https://bioconductor.org/packages/release/bioc/html/topGO.html.

190. Yoon, S., Baik, B., Park, T. & Nam, D. Powerful p-value combination methods to detect incomplete association. *Sci. Rep.* **11**, 6980 (2021).

191. Budden, T. & Bowden, N. A. The Role of Altered Nucleotide Excision Repair and UVB-Induced DNA Damage in Melanomagenesis. *International Journal of Molecular Sciences* **14**, 1132–1151 (2013).

192. Weber, S. Light-driven enzymatic catalysis of DNA repair: a review of recent biophysical studies on photolyase. *Biochimica et Biophysica Acta (BBA) - Bioenergetics* **1707**, 1–23 (2005).

193. Zachayus, A., Loup-Forest, J., Cura, V. & Poterszman, A. Nucleotide Excision Repair: Insights into Canonical and Emerging Functions of the Transcription/DNA Repair Factor TFIIH. *Genes* **16**, 231 (2025).

194. Howard, J. M., Griffis, H.-B., Westendorf, R. & Williams, J. B. The influence of size and abiotic factors on cutaneous water loss. *Advances in Physiology Education* (2020) doi:10.1152/advan.00152.2019.

195. Verberk, W. C. E. P. *et al.* Does oxygen limit thermal tolerance in arthropods? A critical review of current evidence. *Comp. Biochem. Physiol. A Mol. Integr. Physiol.* **192**, 64–78 (2016).

196. Mangum, C. & VAN Winkle, W. Responses of aquatic invertebrates to declining oxygen conditions. *Am. Zool.* **13**, 529–541 (1973).

197. Cheon, S., Zhang, J. & Park, C. Is phylotranscriptomics as reliable as phylogenomics? *Mol. Biol. Evol.* **37**, 3672–3683 (2020).

198. Grabherr, M. G. *et al.* Full-length transcriptome assembly from RNA-Seq data without a reference genome. *Nature Biotechnology* **29**, 644–652 (2011).

199. Bolger, A. M., Lohse, M. & Usadel, B. Trimmomatic: a flexible trimmer for Illumina sequence data. *Bioinformatics* **30**, 2114–2120 (2014).

200. Li, W. & Godzik, A. Cd-hit: a fast program for clustering and comparing large sets of protein or nucleotide sequences. *Bioinformatics* **22**, 1658–1659 (2006).

201. Manni, M., Berkeley, M. R., Seppey, M., Simão, F. A. & Zdobnov, E. M. BUSCO update: Novel and streamlined workflows along with broader and deeper phylogenetic coverage for scoring of eukaryotic, prokaryotic, and viral genomes. *Mol. Biol. Evol.* **38**, 4647–4654 (2021).

202. Patro, R., Duggal, G., Love, M. I., Irizarry, R. A. & Kingsford, C. Salmon provides fast and bias-aware quantification of transcript expression. *Nat. Methods* **14**, 417–419 (2017).

203. Love, M. I., Huber, W. & Anders, S. Moderated estimation of fold change and dispersion for RNA-seq data with DESeq2. *Genome Biol.* **15**, 550 (2014).

204. Ritchie, M. E. *et al.* limma powers differential expression analyses for RNA-sequencing and microarray studies. *Nucleic Acids Res.* **43**, e47 (2015).

205. Langfelder, P. & Horvath, S. WGCNA: an R package for weighted correlation network

analysis. *BMC Bioinformatics* **9**, 559 (2008).

206. Almeida-Silva, F. & Venancio, T. M. BioNERO: an all-in-one R/Bioconductor package for comprehensive and easy biological network reconstruction. *Funct. Integr. Genomics* **22**, 131–136 (2022).

207. García-Vernet, R. *et al.* A proteo-transcriptomic investigation of toxin evolution in planarians and their role in flatworm terrestrialization. *Evolutionary Biology* (2025).

208. Chiva, C. *et al.* QCloud: A cloud-based quality control system for mass spectrometry-based proteomics laboratories. *PLoS One* **13**, e0189209 (2018).

209. Letunic, I. & Bork, P. Interactive Tree of Life (iTOL) v6: recent updates to the phylogenetic tree display and annotation tool. *Nucleic Acids Res.* **52**, W78–W82 (2024).

210. Krassowski, M., Arts, M., Lagger, C. & Max. *Krassowski/complex-Upset: v1.3.5*. (Zenodo, 2022). doi:10.5281/ZENODO.3700590.

211. Kanehisa, M. & Sato, Y. KEGG Mapper for inferring cellular functions from protein sequences. *Protein Sci* **29**, 28–35 (2020).

212. Kanehisa, M., Sato, Y. & Morishima, K. BlastKOALA and GhostKOALA: KEGG Tools for Functional Characterization of Genome and Metagenome Sequences. *J Mol Biol* **428**, 726–731 (2016).

213. Cantalapiedra, C. P., Hernández-Plaza, A., Letunic, I., Bork, P. & Huerta-Cepas, J. EggNOG-mapper v2: Functional annotation, orthology assignments, and domain prediction at the metagenomic scale. *Mol. Biol. Evol.* **38**, 5825–5829 (2021).

214. Benjamin, K. J. M., Katipalli, T. & Paquola, A. C. M. dRFEtools: dynamic recursive feature elimination for omics. *Bioinformatics* **39**, btad513 (2023).

215. Nguyen, H.-N. & Ohn, S.-Y. DRFE: Dynamic recursive feature elimination for gene identification based on random forest. in *Lecture Notes in Computer Science* 1–10 (Springer Berlin Heidelberg, Berlin, Heidelberg, 2006).

216. Hu, Y. *et al.* PANGEA: a new gene set enrichment tool for Drosophila and common research organisms. *Nucleic Acids Res.* **51**, W419–W426 (2023).

Acknowledgements: We thank Luana Da Costa Monteiro, Nicholas Stroustrup and the Planarian Lab from Universitat de Barcelona for kindly providing nematode and planarian samples to initiate the cultures used in the stress experiments; Koryu Kin and Gonzalo Berceo for letting us use their HypoxiLab for the hypoxia experiments; Salvatore Cosentino for his assistance in the installation and bug fixing of SonicParanoid2; Antonis Rokas, who, convergently with AB, suggested the use of machine learning in this work; and Leandro Aristide and Lisandra Benítez-Álvarez for sharing with us their scripts for plotting the mirror trees. The CRG/UPF Proteomics Unit is part of the Spanish Infrastructure for Omics Technologies (ICTS OmicsTech). We also thank Centro de Supercomputación de Galicia (CESGA), particularly Pablo Rey for his assistance and guidance, and the HPC Drago from the Centro Superior de Investigaciones Científicas for access to computer resources. ChatGPT was used to polish grammar and clarity.

Funding:

Secretaria d'Universitats i Recerca del Departament d'Empresa i Coneixement de la Generalitat de Catalunya and ESF Investing in your future grant 2021 FI_B 00476 (GIMR)

Beatriu de Pinós fellowship from Secretaria d'Universitats i Recerca del Departament de Recerca i Universitats of the Generalitat de Catalunya Ref. BP 2021 00035 (FÁFÁ)

Ramón y Cajal fellowship Ref. RYC2023-043494-I (FÁFÁ)

MCIN/AEI /10.13039/501100011033 and FSE+ grant CEX2024-001494-S (FÁFÁ)

Spanish Ministry of Universities and the European Union Next Generation EU/PRTR Margarita Salas grant (RGV)

European Research Council (ERC) under the European Union's Horizon 2020 research and innovation programme grant agreement no. 948281 (RF)

European Commission's Horizon Europe Research and Innovation programme grant agreement no. 101129751 OSCARS project (RF)

Secretaria d'Universitats i Recerca del Departament d'Economia i Coneixement de la Generalitat de Catalunya AGAUR 2021-SGR00420 (RF)

Author contributions:

Conceptualization: GIMR, KE, RF

Specimens collection in fieldwork expeditions: FÁFÁ, KE, GIMR, JSO, IR, RGV, RF

Gene repertoire evolution analysis: GIMR

Transcriptomic and gene co-expression network analyses: KE

Stress experiments: KE, JSO, NE

Wet lab experiments: JSO, NE

Machine learning analysis: GIMR, AB

Proteomics analyses: JPG, RGV, LR, CC, ES

Computational analyses assistance: BC, CVC

Interpretation and discussion: GIMR, KE, RF

Visualization: GIMR, KE, CVC, BC

Computational resources: AB, RF

Funding acquisition: RF

Supervision: RF

Writing – original draft: GIMR, KE, RF

Writing – review & editing: GIMR, KE, JSO, NE, FÁFÁ, BC, CVC, RGV, JPG, LR, IR, CC, ES, AB, RF

Competing interests:

Authors declare that they have no competing interests.

Data and Materials Availability:

RNA-seq and IsoSeq raw data are available at the SRA NCBI repository, under BioProject XXXXXX (*to be provided*). Mass spectrometry proteomics data is available

in ProteomeXchange Consortium via PRIDE under accession number PXDXXXXX (*to be provided*). Output files for all main analyses are available at Figshare: https://figshare.com/s/90da0d7fbd3afdd6d5c0 (*10.6084/m9.figshare.29210009*). All code and customs scripts are available at the GitHub repository associated to this manuscript https://github.com/MetazoaPhylogenomicsLab/Martinez-Redondo-Eleftheriadi_et_al_2025_Genomic_basis_animal_terrestrialisation (*final DOI to be provided*).

Tables S1 to S72 can be found in the following file: https://docs.google.com/spreadsheets/d/182PcH37zYyzkvPv_H1NaFGw_cs0nnTmxHee15Ok9tdw/edit?usp=drive_link

Supplementary Materials

Headers for tables S1 to S72

Figs. S1 to S290

Supplementary Tables S1 to S72 can be found in the following file: https://docs.google.com/spreadsheets/d/182PcH37zYyzkvPv_H1NaFGw_cs0nnTmxHee15Ok9tdw/edit?usp=drive_link

Table S1. Species used in the present study, including their species codes used in the analyses, taxonomic and habitat information, the proteome data source (i.e., transcriptome, genome, or IsoSeq), and whether it was used in stress experiments.

Table S2. OGs gained and lost at each terrestrialization event. Events defined only by one species are included, with the number of species-specific genes in parentheses.

Table S3. Summary statistics of experimental RNA-seq data for *C. elegans* before and after preprocessing of reads, including the percentage of mapping to the de novo reference transcriptome.

Table S4. Summary statistics of experimental RNA-seq data for *L. marina* before and after preprocessing of reads, including the percentage of mapping to the de novo reference transcriptome.

Table S5. Summary statistics of experimental RNA-seq data for *P. aurorbis* before and after preprocessing of reads, including the percentage of mapping to the de novo reference transcriptome.

Table S6. Summary statistics of experimental RNA-seq data for *P. laevis* before and after preprocessing of reads, including the percentage of mapping to the de novo reference transcriptome.

Table S7. Summary statistics of experimental RNA-seq data for *L. oceanica* before and after preprocessing of reads, including the percentage of mapping to the de novo reference transcriptome.

Table S8. Summary statistics of experimental RNA-seq data for *O. nungara* before and after preprocessing of reads, including the percentage of mapping to the de novo reference transcriptome.

Table S9. Summary statistics of experimental RNA-seq data for *S. mediterranea* before and after preprocessing of reads, including the percentage of mapping to the de novo reference transcriptome.

Table S10. Summary statistics of experimental RNA-seq data for *P. turbinatus* before and after preprocessing of reads, including the percentage of mapping to the de novo reference transcriptome.

Table S11. Summary statistics of experimental RNA-seq data for *S. pectinata* before and after preprocessing of reads, including the percentage of mapping to the de novo reference transcriptome.

Table S12. Summary statistics of experimental RNA-seq data for *T. pisana* before and after preprocessing of reads, including the percentage of mapping to the de novo reference transcriptome.

Table S13. Summary statistics of experimental RNA-seq data for *P. acuta* before and after preprocessing of reads, including the percentage of mapping to the de novo reference transcriptome.

Table S14. Summary statistics of experimental RNA-seq data for *A. marina* before and after preprocessing of reads, including the percentage of mapping to the de novo reference transcriptome.

Table S15. Summary statistics of experimental RNA-seq data for *E. andrei* before and after preprocessing of reads, including the percentage of mapping to the de novo reference transcriptome.

Table S16. Summary statistics of experimental RNA-seq data for *H. medicinalis* before and after preprocessing of reads, including the percentage of mapping to the de novo reference transcriptome.

Table S17. Summary statistics of experimental RNA-seq data for *L. chalicophora* before and after preprocessing of reads, including the percentage of mapping to the de novo reference transcriptome.

Table S18. Summary statistics of experimental RNA-seq data for *T. melanocephalum* before and after preprocessing of reads, including the percentage of mapping to the de novo reference transcriptome.

Table S19. Summary statistics of experimental RNA-seq data for *T. longissimum* before and after preprocessing of reads, including the percentage of mapping to the de novo reference transcriptome.

Table S20. Summary statistics of experimental PacBio Iso-Seq data and de novo transcriptome assembly metrics for each species. Key statistics include the number of sequencing runs, total HiFi reads, yield, mean read length, read quality, number of transcripts after CD-HIT clustering, BUSCO completeness scores (metazoa_odb10), and number of predicted longest isoform proteins. One species (*S. pectinata*) was assembled using Illumina reads and Trinity due to lack of Iso-Seq data.

Table S21. Scale-free topology (SFT) analysis parameters for species-specific WGCNA. The table includes the R^2 threshold used to assess scale-free topology fit, the soft-thresholding power (β) selected to approximate a scale-free network, and the resulting mean connectivity. In cases where no satisfactory SFT fit ($R^2 \geq 0.8$) was achieved, a default β value of 6 was applied as recommended by WGCNA guidelines.

Table S22. Statistically significant gene co-expression modules identified in *C. elegans* across experimental conditions.

Table S23. Statistically significant gene co-expression modules identified in *L. marina* across experimental conditions.

Table S24. Statistically significant gene co-expression modules identified in *P. aurorbis* across experimental conditions.

Table S25. Statistically significant gene co-expression modules identified in *P. laevis* across experimental conditions.

Table S26. Statistically significant gene co-expression modules identified in *L. oceanica* across experimental conditions.

Table S27. Statistically significant gene co-expression modules identified in *O. nungara* across experimental conditions.

Table S28. Statistically significant gene co-expression modules identified in *S. mediterranea* across experimental conditions.

Table S29. Statistically significant gene co-expression modules identified in *P. turbinatus* across experimental conditions.

Table S30. Statistically significant gene co-expression modules identified in *S. pectinata* across experimental conditions.

Table S31. Statistically significant gene co-expression modules identified in *T. pisana* across experimental conditions.

Table S32. Statistically significant gene co-expression modules identified in *P. acuta* across experimental conditions.

Table S33. Statistically significant gene co-expression modules identified in *A. marina* across experimental conditions.

Table S34. Statistically significant gene co-expression modules identified in *E. andrei* across experimental conditions.

Table S35. Statistically significant gene co-expression modules identified in *H. medicinalis* across experimental conditions.

Table S36. Statistically significant gene co-expression modules identified in *L. chalicophora* across experimental conditions.

Table S37. Statistically significant gene co-expression modules identified in *T. melanocephalum* across experimental conditions.

Table S38. Statistically significant gene co-expression modules identified in *T. longissimum* across experimental conditions.

Table S39. Hub genes from statistically significant WGCNA modules per experimental condition in *C. elegans*.

Table S40. Hub genes from statistically significant WGCNA modules per experimental condition in *L. marina*.

Table S41. Hub genes from statistically significant WGCNA modules per experimental condition in *P. aurorbis*.

Table S42. Hub genes from statistically significant WGCNA modules per experimental condition in *P. laevis*.

Table S43. Hub genes from statistically significant WGCNA modules per experimental condition in *L. oceanica*.

Table S44. Hub genes from statistically significant WGCNA modules per experimental condition in *O. nungara*.

Table S45. Hub genes from statistically significant WGCNA modules per experimental condition in *S. mediterranea*.

Table S46. Hub genes from statistically significant WGCNA modules per experimental condition in *P. turbinatus*.

Table S47. Hub genes from statistically significant WGCNA modules per experimental condition in *S. pectinata*.

Table S48. Hub genes from statistically significant WGCNA modules per experimental condition in *T. pisana*.

Table S49. Hub genes from statistically significant WGCNA modules per experimental condition in *P. acuta*.

Table S50. Hub genes from statistically significant WGCNA modules per experimental condition in *A. marina*.

Table S51. Hub genes from statistically significant WGCNA modules per experimental condition in *E. andrei*.

Table S52. Hub genes from statistically significant WGCNA modules per experimental condition in *H. medicinalis*.

Table S53. Hub genes from statistically significant WGCNA modules per experimental condition in *L. chalicophora*.

Table S54. Hub genes from statistically significant WGCNA modules per experimental condition in *T. melanocephalum*.

Table S55. Hub genes from statistically significant WGCNA modules per experimental condition in *T. longissimum*.

Table S56. Proportions of hub - containing orthogroups per experimental condition across species.

Table S57. Functional annotations of 42 non-hub containing orthogroups shared across all 17 species exposed to abiotic stressors using BLASTp and KEGG Mapper. Each row represents a gene within one of the 42 orthogroups. Protein functions were inferred via BLASTp searches against the NCBI non-redundant protein database and functionally classified using KEGG Mapper. Annotations corresponding to uninformative hypothetical proteins or redundant entries were excluded.

Table S58. Clusters of hub-containing orthogroups grouped by Gene Ontology terms using constellatoR for experiment CD. Habitat refers to species used in the experiments only; OGs may include additional species. “Aquatic” indicates clusters with hubs from aquatic species, “Terrestrial” from terrestrial species, and “Mixed” includes hubs from both.

Table S59. Clusters of hub-containing orthogroups grouped by Gene Ontology terms using constellatoR for experiment CF. Habitat refers to species used in the experiments only; OGs may include additional species. “Aquatic” indicates clusters with hubs from aquatic species, “Terrestrial” from terrestrial species, and “Mixed” includes hubs from both.

Table S60. Clusters of hub-containing orthogroups grouped by Gene Ontology terms using constellatoR for experiment Hyper. Habitat refers to species used in the experiments only; OGs may include additional species. “Aquatic” indicates clusters with hubs from aquatic species, “Terrestrial” from terrestrial species, and “Mixed” includes hubs from both.

Table S61. Clusters of hub-containing orthogroups grouped by Gene Ontology terms using constellatoR for experiment Hypo. Habitat refers to species used in the experiments only; OGs may include additional species. “Aquatic” indicates clusters with hubs from aquatic species, “Terrestrial” from terrestrial species, and “Mixed” includes hubs from both.

Table S62. Clusters of hub-containing orthogroups grouped by Gene Ontology terms using constellatoR for experiment OR. Habitat refers to species used in the experiments only; OGs may include additional species. “Aquatic” indicates clusters with hubs from aquatic species, “Terrestrial” from terrestrial species, and “Mixed” includes hubs from both.

Table S63. Clusters of hub-containing orthogroups grouped by Gene Ontology terms using constellatoR for experiment UV0. Habitat refers to species used in the experiments only; OGs may include additional species. “Aquatic” indicates clusters with hubs from aquatic species, “Terrestrial” from terrestrial species, and “Mixed” includes hubs from both.

Table S64. Clusters of hub-containing orthogroups grouped by Gene Ontology terms using constellatoR for experiment UV15D. Habitat refers to species used in the experiments only; OGs may include additional species. “Aquatic” indicates clusters with hubs from aquatic species, “Terrestrial” from terrestrial species, and “Mixed” includes hubs from both.

Table S65. Clusters of hub-containing orthogroups grouped by Gene Ontology terms using constellatoR for experiment UV15L. Habitat refers to species used in the experiments only; OGs may include additional species. “Aquatic” indicates clusters with hubs from aquatic species, “Terrestrial” from terrestrial species, and “Mixed” includes hubs from both.

Table S66. Clusters of hub-containing orthogroups grouped by Gene Ontology terms using constellatoR for experiment UV24D. Habitat refers to species used in the experiments only; OGs may include additional species. “Aquatic” indicates clusters with hubs from aquatic species, “Terrestrial” from terrestrial species, and “Mixed” includes hubs from both.

Table S67. Clusters of hub-containing orthogroups grouped by Gene Ontology terms using constellatoR for experiment UV24L. Habitat refers to species used in the experiments only; OGs may include additional species. “Aquatic” indicates clusters with hubs from aquatic species, “Terrestrial” from terrestrial species, and “Mixed” includes hubs from both.

Table S68. Clusters of hub-containing orthogroups grouped by Gene Ontology terms using constellatoR for experiment VL. Habitat refers to species used in the experiments only; OGs may include additional species. “Aquatic” indicates clusters with hubs from aquatic species, “Terrestrial” from terrestrial species, and “Mixed” includes hubs from both.

Table S69. Top 130 OGs inferred by the Machine Learning model. Information on the model ranking, function (BLASTp, PANGEA pathways, and FANTASIA GO terms), number of species and sequences of OGs, their age of origin, together with stress-experiments information (whether hub genes are contained, how many, in which species, and which experiments).

Table S70. Species sampled for the study, including habitat type, sampling coordinates, locality information, and permitting status. Coordinates refer to new sample collection points.

Table S71. Summary of the proteomics statistics for each species. MP #1 Unique peptides indicates the number of master proteins with at least 1 Unique peptide. MP#1 in at least 2 replicates indicates the number of Master Proteins that are detected in at least 2 out of 3 replicates. MP#1 without contaminants indicates the final number of master proteins after removing the contaminants detected through LC-MS.

Table S72. Species-specific experimental conditions.

Supplementary Figures can be found in the following file: **https://drive.google.com/file/d/11vlI54GKr_McV-S4Xgi1EY4IMG-lyw7d/view?usp=drive_link**

Figure S1. Treemap showing semantic similarity-based clustering of enriched Biological Process GO terms of OGs gained in Hexapoda.

Figure S2. Treemap showing semantic similarity-based clustering of enriched Molecular Function GO terms of OGs gained in Hexapoda.

Figure S3. Treemap showing semantic similarity-based clustering of enriched Cellular Component GO terms of OGs gained in Hexapoda.

Figure S4. Treemap showing semantic similarity-based clustering of enriched Biological Process GO terms of OGs lost in Hexapoda.

Figure S5. Treemap showing semantic similarity-based clustering of enriched Molecular Function GO terms of OGs lost in Hexapoda.

Figure S6. Treemap showing semantic similarity-based clustering of enriched Cellular Component GO terms of OGs lost in Hexapoda.

Figure S7. Treemap showing semantic similarity-based clustering of enriched Biological Process GO terms of OGs gained in Coenobitidae (Anomura).

Figure S8. Treemap showing semantic similarity-based clustering of enriched Molecular Function GO terms of OGs gained in Coenobitidae (Anomura).

Figure S9. Treemap showing semantic similarity-based clustering of enriched Cellular Component GO terms of OGs gained in Coenobitidae (Anomura).

Figure S10. Treemap showing semantic similarity-based clustering of enriched Biological Process GO terms of OGs lost in Coenobitidae (Anomura).

Figure S11. Treemap showing semantic similarity-based clustering of enriched Molecular Function GO terms of OGs lost in Coenobitidae (Anomura).

Figure S12. Treemap showing semantic similarity-based clustering of enriched Cellular Component GO terms of OGs lost in Coenobitidae (Anomura).

Figure S13. Treemap showing semantic similarity-based clustering of enriched Biological Process GO terms of OGs gained in Gecarcinidae (Brachyura).

Figure S14. Treemap showing semantic similarity-based clustering of enriched Molecular Function GO terms of OGs gained in Gecarcinidae (Brachyura).

Figure S15. Treemap showing semantic similarity-based clustering of enriched Cellular Component GO terms of OGs gained in Gecarcinidae (Brachyura).

Figure S16. Treemap showing semantic similarity-based clustering of enriched Biological Process GO terms of OGs lost in Gecarcinidae (Brachyura).

Figure S17. Treemap showing semantic similarity-based clustering of enriched Molecular Function GO terms of OGs lost in Gecarcinidae (Brachyura).

Figure S18. Treemap showing semantic similarity-based clustering of enriched Cellular Component GO terms of OGs lost in Gecarcinidae (Brachyura).

Figure S19. Treemap showing semantic similarity-based clustering of enriched Biological Process GO terms of OGs gained in Isopoda.

Figure S20. Treemap showing semantic similarity-based clustering of enriched Molecular Function GO terms of OGs gained in Isopoda.

Figure S21. Treemap showing semantic similarity-based clustering of enriched Cellular Component GO terms of OGs gained in Isopoda.

Figure S22. Treemap showing semantic similarity-based clustering of enriched Biological Process GO terms of OGs lost in Isopoda.

Figure S23. Treemap showing semantic similarity-based clustering of enriched Molecular Function GO terms of OGs lost in Isopoda.

Figure S24. Treemap showing semantic similarity-based clustering of enriched Cellular Component GO terms of OGs lost in Isopoda.

Figure S25. Treemap showing semantic similarity-based clustering of enriched Biological Process GO terms of OGs gained in Myriapoda.

Figure S26. Treemap showing semantic similarity-based clustering of enriched Molecular Function GO terms of OGs gained in Myriapoda.

Figure S27. Treemap showing semantic similarity-based clustering of enriched Cellular Component GO terms of OGs gained in Myriapoda.

Figure S28. Treemap showing semantic similarity-based clustering of enriched Biological Process GO terms of OGs lost in Myriapoda.

Figure S29. Treemap showing semantic similarity-based clustering of enriched Molecular Function GO terms of OGs lost in Myriapoda.

Figure S30. Treemap showing semantic similarity-based clustering of enriched Cellular Component GO terms of OGs lost in Myriapoda.

Figure S31. Treemap showing semantic similarity-based clustering of enriched Biological Process GO terms of OGs gained in Arachnida.

Figure S32. Treemap showing semantic similarity-based clustering of enriched Molecular Function GO terms of OGs gained in Arachnida.

Figure S33. Treemap showing semantic similarity-based clustering of enriched Cellular Component GO terms of OGs gained in Arachnida.

Figure S34. Treemap showing semantic similarity-based clustering of enriched Biological Process GO terms of OGs lost in Arachnida.

Figure S35. Treemap showing semantic similarity-based clustering of enriched Molecular Function GO terms of OGs lost in Arachnida.

Figure S36. Treemap showing semantic similarity-based clustering of enriched Cellular Component GO terms of OGs lost in Arachnida.

Figure S37. Treemap showing semantic similarity-based clustering of enriched Biological Process GO terms of OGs gained in Onychophora.

Figure S38. Treemap showing semantic similarity-based clustering of enriched Molecular Function GO terms of OGs gained in Onychophora.

Figure S39. Treemap showing semantic similarity-based clustering of enriched Cellular Component GO terms of OGs gained in Onychophora.

Figure S40. Treemap showing semantic similarity-based clustering of enriched Biological Process GO terms of OGs lost in Onychophora.

Figure S41. Treemap showing semantic similarity-based clustering of enriched Molecular Function GO terms of OGs lost in Onychophora.

Figure S42. Treemap showing semantic similarity-based clustering of enriched Cellular Component GO terms of OGs lost in Onychophora.

Figure S43. Treemap showing semantic similarity-based clustering of enriched Biological Process GO terms of OGs gained in Eutardigrada.

Figure S44. Treemap showing semantic similarity-based clustering of enriched Molecular Function GO terms of OGs gained in Eutardigrada.

Figure S45. Treemap showing semantic similarity-based clustering of enriched Cellular Component GO terms of OGs gained in Eutardigrada.

Figure S46. Treemap showing semantic similarity-based clustering of enriched Biological Process GO terms of OGs lost in Eutardigrada.

Figure S47. Treemap showing semantic similarity-based clustering of enriched Molecular Function GO terms of OGs lost in Eutardigrada.

Figure S48. Treemap showing semantic similarity-based clustering of enriched Cellular Component GO terms of OGs lost in Eutardigrada.

Figure S49. Treemap showing semantic similarity-based clustering of enriched Biological Process GO terms of OGs gained in Rhabditida.

Figure S50. Treemap showing semantic similarity-based clustering of enriched Molecular Function GO terms of OGs gained in Rhabditida.

Figure S51. Treemap showing semantic similarity-based clustering of enriched Cellular Component GO terms of OGs gained in Rhabditida.

Figure S52. Treemap showing semantic similarity-based clustering of enriched Biological Process GO terms of OGs lost in Rhabditida.

Figure S53. Treemap showing semantic similarity-based clustering of enriched Molecular Function GO terms of OGs lost in Rhabditida.

Figure S54. Treemap showing semantic similarity-based clustering of enriched Cellular Component GO terms of OGs lost in Rhabditida.

Figure S55. Treemap showing semantic similarity-based clustering of enriched Biological Process GO terms of OGs gained in Stylommatophora.

Figure S56. Treemap showing semantic similarity-based clustering of enriched Molecular Function GO terms of OGs gained in Stylommatophora.

Figure S57. Treemap showing semantic similarity-based clustering of enriched Cellular Component GO terms of OGs gained in Stylommatophora.

Figure S58. Treemap showing semantic similarity-based clustering of enriched Biological Process GO terms of OGs lost in Stylommatophora.

Figure S59. Treemap showing semantic similarity-based clustering of enriched Molecular Function GO terms of OGs lost in Stylommatophora.

Figure S60. Treemap showing semantic similarity-based clustering of enriched Cellular Component GO terms of OGs lost in Stylommatophora.

Figure S61. Treemap showing semantic similarity-based clustering of enriched Biological Process GO terms of OGs gained in Ellobiida.

Figure S62. Treemap showing semantic similarity-based clustering of enriched Molecular Function GO terms of OGs gained in Ellobiida.

Figure S63. Treemap showing semantic similarity-based clustering of enriched Cellular Component GO terms of OGs gained in Ellobiida.

Figure S64. Treemap showing semantic similarity-based clustering of enriched Biological Process GO terms of OGs lost in Ellobiida.

Figure S65. Treemap showing semantic similarity-based clustering of enriched Molecular Function GO terms of OGs lost in Ellobiida.

Figure S66. Treemap showing semantic similarity-based clustering of enriched Cellular Component GO terms of OGs lost in Ellobiida.

Figure S67. Treemap showing semantic similarity-based clustering of enriched Biological Process GO terms of OGs gained in Crassiclitellata.

Figure S68. Treemap showing semantic similarity-based clustering of enriched Molecular Function GO terms of OGs gained in Crassiclitellata.

Figure S69. Treemap showing semantic similarity-based clustering of enriched Cellular Component GO terms of OGs gained in Crassiclitellata.

Figure S70. Treemap showing semantic similarity-based clustering of enriched Biological Process GO terms of OGs lost in Crassiclitellata.

Figure S71. Treemap showing semantic similarity-based clustering of enriched Molecular Function GO terms of OGs lost in Crassiclitellata.

Figure S72. Treemap showing semantic similarity-based clustering of enriched Cellular Component GO terms of OGs lost in Crassiclitellata.

Figure S73. Treemap showing semantic similarity-based clustering of enriched Biological Process GO terms of OGs gained in Acteonemertidae.

Figure S74. Treemap showing semantic similarity-based clustering of enriched Molecular Function GO terms of OGs gained in Acteonemertidae.

Figure S75. Treemap showing semantic similarity-based clustering of enriched Cellular Component GO terms of OGs gained in Acteonemertidae.

Figure S76. Treemap showing semantic similarity-based clustering of enriched Biological Process GO terms of OGs lost in Acteonemertidae.

Figure S77. Treemap showing semantic similarity-based clustering of enriched Molecular Function GO terms of OGs lost in Acteonemertidae.

Figure S78. Treemap showing semantic similarity-based clustering of enriched Cellular Component GO terms of OGs lost in Acteonemertidae.

Figure S79. Treemap showing semantic similarity-based clustering of enriched Biological Process GO terms of OGs gained in Geoplanidae.

Figure S80. Treemap showing semantic similarity-based clustering of enriched Molecular Function GO terms of OGs gained in Geoplanidae.

Figure S81. Treemap showing semantic similarity-based clustering of enriched Cellular Component GO terms of OGs gained in Geoplanidae.

Figure S82. Treemap showing semantic similarity-based clustering of enriched Biological Process GO terms of OGs lost in Geoplanidae.

Figure S83. Treemap showing semantic similarity-based clustering of enriched Molecular Function GO terms of OGs lost in Geoplanidae.

Figure S84. Treemap showing semantic similarity-based clustering of enriched Cellular Component GO terms of OGs lost in Geoplanidae.

Figure S85. Treemap showing semantic similarity-based clustering of enriched Biological Process GO terms of OGs gained in Tetrapoda.

Figure S86. Treemap showing semantic similarity-based clustering of enriched Molecular Function GO terms of OGs gained in Tetrapoda.

Figure S87. Treemap showing semantic similarity-based clustering of enriched Cellular Component GO terms of OGs gained in Tetrapoda.

Figure S88. Treemap showing semantic similarity-based clustering of enriched Biological Process GO terms of OGs lost in Tetrapoda.

Figure S89. Treemap showing semantic similarity-based clustering of enriched Molecular Function GO terms of OGs lost in Tetrapoda.

Figure S90. Treemap showing semantic similarity-based clustering of enriched Cellular Component GO terms of OGs lost in Tetrapoda.

Figure S91. Gained and lost orthogroups at terrestrialisation nodes. a, Semantic similarity matrix of GO terms from orthogroups (OGs) gained. **b**, Semantic similarity matrix of GO terms from lost orthogroups. **c**, Cumulative count of orthogroup lost in Myriapoda as number of species increases. **d**, Cumulative count of OGs lost in Onychophora as number of species increases.

Figure S92. Soft-thresholding power selection for WGCNA of *C. elegans*. The left panel shows the scale-free topology model fit (signed R^2) across soft-thresholding powers (β), and the right panel shows the mean connectivity at each β.

Figure S93. Soft-thresholding power selection for WGCNA of *L. marina*. The left panel shows the scale-free topology model fit (signed R^2) across soft-thresholding powers (β), and the right panel shows the mean connectivity at each β.

Figure S94. Soft-thresholding power selection for WGCNA of *P. aurorbis*. The left panel shows the scale-free topology model fit (signed R^2) across soft-thresholding powers (β), and the right panel shows the mean connectivity at each β.

Figure S95. Soft-thresholding power selection for WGCNA of *P. laevis*. The left panel shows the scale-free topology model fit (signed R^2) across soft-thresholding powers (β), and the right panel shows the mean connectivity at each β.

Figure S96. Soft-thresholding power selection for WGCNA of *L. oceanica*. The left panel shows the scale-free topology model fit (signed R^2) across soft-thresholding powers (β), and the right panel shows the mean connectivity at each β.

Figure S97. Soft-thresholding power selection for WGCNA of *O. nungara*. The left panel shows the scale-free topology model fit (signed R^2) across soft-thresholding powers (β), and the right panel shows the mean connectivity at each β.

Figure S98. Soft-thresholding power selection for WGCNA of *S. mediterranea*. The left panel shows the scale-free topology model fit (signed R^2) across soft-thresholding powers (β), and the right panel shows the mean connectivity at each β.

Figure S99. Soft-thresholding power selection for WGCNA of *P. turbinatus*. The left panel shows the scale-free topology model fit (signed R^2) across soft-thresholding powers (β), and the right panel shows the mean connectivity at each β.

Figure S100. Soft-thresholding power selection for WGCNA of *S. pectinata*. The left panel shows the scale-free topology model fit (signed R^2) across soft-thresholding powers (β), and the right panel shows the mean connectivity at each β.

Figure S101. Soft-thresholding power selection for WGCNA of *T. pisana*. The left panel shows the scale-free topology model fit (signed R^2) across soft-thresholding powers (β), and the right panel shows the mean connectivity at each β.

Figure S102. Soft-thresholding power selection for WGCNA of *P. acuta*. The left panel shows the scale-free topology model fit (signed R^2) across soft-thresholding powers (β), and the right panel shows the mean connectivity at each β.

Figure S103. Soft-thresholding power selection for WGCNA of *A. marina*. The left panel shows the scale-free topology model fit (signed R^2) across soft-thresholding powers (β), and the right panel shows the mean connectivity at each β.

Figure S104. Soft-thresholding power selection for WGCNA of *E. andrei*. The left panel shows the scale-free topology model fit (signed R^2) across soft-thresholding powers (β), and the right panel shows the mean connectivity at each β.

Figure S105. Soft-thresholding power selection for WGCNA of *H. medicinalis*. The left panel shows the scale-free topology model fit (signed R^2) across soft-thresholding powers (β), and the right panel shows the mean connectivity at each β.

Figure S106. Soft-thresholding power selection for WGCNA of *L. chalicophora*. The left panel shows the scale-free topology model fit (signed R^2) across soft-thresholding powers (β), and the right panel shows the mean connectivity at each β.

Figure S107. Soft-thresholding power selection for WGCNA of *T. melanocephalum*. The left panel shows the scale-free topology model fit (signed R^2) across soft-thresholding powers (β), and the right panel shows the mean connectivity at each β.

Figure S108. Soft-thresholding power selection for WGCNA of *T. longissimum*. The left panel shows the scale-free topology model fit (signed R^2) across soft-thresholding powers (β), and the right panel shows the mean connectivity at each β.

Figure S109. Module-trait correlations between gene co-expression modules of *C. elegans* and experimental stress conditions. Each row represents a module eigengene, and each column corresponds to a specific stress experiment. Numbers indicate Pearson correlation coefficients (r), with p-values in parentheses. Cell colors range from blue (negative correlation) to red (positive correlation).

Figure S110. Module-trait correlations between gene co-expression modules of *L. marina* and experimental stress conditions. Each row represents a module eigengene, and each column corresponds to a specific stress experiment. Numbers indicate Pearson correlation coefficients (r), with p-values in parentheses. Cell colors range from blue (negative correlation) to red (positive correlation).

Figure S111. Module-trait correlations between gene co-expression modules of *P. aurorbis* and experimental stress conditions. Each row represents a module eigengene, and each column corresponds to a specific stress experiment. Numbers indicate Pearson correlation coefficients (r), with p-values in parentheses. Cell colors range from blue (negative correlation) to red (positive correlation).

Figure S112. Module-trait correlations between gene co-expression modules of *P. laevis* and experimental stress conditions. Each row represents a module eigengene, and each column corresponds to a specific stress experiment. Numbers indicate Pearson correlation coefficients

(r), with p-values in parentheses. Cell colors range from blue (negative correlation) to red (positive correlation).

Figure S113. Module-trait correlations between gene co-expression modules of *L. oceanica* and experimental stress conditions. Each row represents a module eigengene, and each column corresponds to a specific stress experiment. Numbers indicate Pearson correlation coefficients (r), with p-values in parentheses. Cell colors range from blue (negative correlation) to red (positive correlation).

Figure S114. Module-trait correlations between gene co-expression modules of *O. nungara* and experimental stress conditions. Each row represents a module eigengene, and each column corresponds to a specific stress experiment. Numbers indicate Pearson correlation coefficients (r), with p-values in parentheses. Cell colors range from blue (negative correlation) to red (positive correlation).

Figure S115. Module-trait correlations between gene co-expression modules of *S. mediterranea* and experimental stress conditions. Each row represents a module eigengene, and each column corresponds to a specific stress experiment. Numbers indicate Pearson correlation coefficients (r), with p-values in parentheses. Cell colors range from blue (negative correlation) to red (positive correlation).

Figure S116. Module-trait correlations between gene co-expression modules of *P. turbinatus* and experimental stress conditions. Each row represents a module eigengene, and each column corresponds to a specific stress experiment. Numbers indicate Pearson correlation coefficients (r), with p-values in parentheses. Cell colors range from blue (negative correlation) to red (positive correlation).

Figure S117. Module-trait correlations between gene co-expression modules of *S. pectinata* and experimental stress conditions. Each row represents a module eigengene, and each column corresponds to a specific stress experiment. Numbers indicate Pearson correlation coefficients (r), with p-values in parentheses. Cell colors range from blue (negative correlation) to red (positive correlation).

Figure S118. Module-trait correlations between gene co-expression modules of *T. pisana* and experimental stress conditions. Each row represents a module eigengene, and each column corresponds to a specific stress experiment. Numbers indicate Pearson correlation coefficients (r), with p-values in parentheses. Cell colors range from blue (negative correlation) to red (positive correlation).

Figure S119. Module-trait correlations between gene co-expression modules of *P. acuta* and experimental stress conditions. Each row represents a module eigengene, and each column corresponds to a specific stress experiment. Numbers indicate Pearson correlation coefficients (r), with p-values in parentheses. Cell colors range from blue (negative correlation) to red (positive correlation).

Figure S120. Module-trait correlations between gene co-expression modules of *A. marina* and experimental stress conditions. Each row represents a module eigengene, and each column corresponds to a specific stress experiment. Numbers indicate Pearson correlation coefficients (r), with p-values in parentheses. Cell colors range from blue (negative correlation) to red (positive correlation).

Figure S121. Module-trait correlations between gene co-expression modules of *E. andrei* and experimental stress conditions. Each row represents a module eigengene, and each column corresponds to a specific stress experiment. Numbers indicate Pearson correlation coefficients (r), with p-values in parentheses. Cell colors range from blue (negative correlation) to red (positive correlation).

Figure S122. Module-trait correlations between gene co-expression modules of *H. medicinalis* and experimental stress conditions. Each row represents a module eigengene, and each column corresponds to a specific stress experiment. Numbers indicate Pearson correlation coefficients (r), with p-values in parentheses. Cell colors range from blue (negative correlation) to red (positive correlation).

Figure S123. Module-trait correlations between gene co-expression modules of *L. chalicophora* and experimental stress conditions. Each row represents a module eigengene, and each column corresponds to a specific stress experiment. Numbers indicate Pearson correlation coefficients (r), with p-values in parentheses. Cell colors range from blue (negative correlation) to red (positive correlation).

Figure S124. Module-trait correlations between gene co-expression modules of *T. melanocephalum* and experimental stress conditions. Each row represents a module eigengene, and each column corresponds to a specific stress experiment. Numbers indicate Pearson correlation coefficients (r), with p-values in parentheses. Cell colors range from blue (negative correlation) to red (positive correlation).

Figure S125. Module-trait correlations between gene co-expression modules of *T. longissimum* and experimental stress conditions. Each row represents a module eigengene, and each column corresponds to a specific stress experiment. Numbers indicate Pearson correlation coefficients (r), with p-values in parentheses. Cell colors range from blue (negative correlation) to red (positive correlation).

Figure S126. Upset plot showing overlap of all orthogroups (not only hub-containing) resulting from species-specific co-expression networks. Dots connect species that have a number of orthogroups in common, the number indicated in each bar from the barplot on top. Only 42 orthogroups out of ca. 540.000 were shared among all species.

Figure S127. Functional convergence of species-specific, GO-annotated hub genes across animal lineages under the remaining stress conditions. Constellation plots of functions of hub genes across 17 aquatic and terrestrial species for each experimental condition. Each polygon represents a distinct functional cluster formed by species with

similar GO annotations, despite no orthogroup-level overlap across species. Cluster exemplars indicate the species that act as centroid in each cluster. The presence of hub genes from multiple species within the same functional cluster demonstrates convergence in stress-response roles across independent lineages.

Figure S128. Functional convergence of species-specific KEGG pathways across animal lineages under stress conditions. a, Heatmaps showing the presence/absence of KEGG pathways in hub gene sets under abiotic stress conditions**.** Each row represents a KEGG pathway, and each column corresponds to a species. The left heatmap displays a summary heatmap including only pathways that are present in at least 80% of species, considering all experimental conditions combined. On the right, separate heatmaps are shown for each experimental condition, filtered by the same set of pathways (rows) as in the summary heatmap. **b**, Top 10 pathways per experiment.

Figure S129. Pathway presence/absence for experiment CD.

Figure S130. Pathway presence/absence for experiment CF.

Figure S131. Pathway presence/absence for experiment Hyper.

Figure S132. Pathway presence/absence for experiment Hypo.

Figure S133. Pathway presence/absence for experiment OR.

Figure S134. Pathway presence/absence for experiment UV0.

Figure S135. Pathway presence/absence for experiment UV15D.

Figure S136. Pathway presence/absence for experiment UV15L.

Figure S137. Pathway presence/absence for experiment UV24D.

Figure S138. Pathway presence/absence for experiment UV24L.

Figure S139. Pathway presence/absence for experiment VL.

Figure S140. Species tree showing the origin (orange dot), losses (pink dots), and gene count (black bars on the outer side) per species for OG 2.

Figure S141. Species tree showing the origin (orange dot), losses (pink dots), and gene count (black bars on the outer side) per species for OG 6.

Figure S142. Species tree showing the origin (orange dot), losses (pink dots), and gene count (black bars on the outer side) per species for OG 7.

Figure S143. Species tree showing the origin (orange dot), losses (pink dots), and gene count (black bars on the outer side) per species for OG 9.

Figure S144. Species tree showing the origin (orange dot), losses (pink dots), and gene count (black bars on the outer side) per species for OG 14.

Figure S145. Species tree showing the origin (orange dot), losses (pink dots), and gene count (black bars on the outer side) per species for OG 23.

Figure S146. Species tree showing the origin (orange dot), losses (pink dots), and gene count (black bars on the outer side) per species for OG 29.

Figure S147. Species tree showing the origin (orange dot), losses (pink dots), and gene count (black bars on the outer side) per species for OG 37.

Figure S148. Species tree showing the origin (orange dot), losses (pink dots), and gene count (black bars on the outer side) per species for OG 53.

Figure S149. Species tree showing the origin (orange dot), losses (pink dots), and gene count (black bars on the outer side) per species for OG 63.

Figure S150. Species tree showing the origin (orange dot), losses (pink dots), and gene count (black bars on the outer side) per species for OG 74.

Figure S151. Species tree showing the origin (orange dot), losses (pink dots), and gene count (black bars on the outer side) per species for OG 96.

Figure S152. Species tree showing the origin (orange dot), losses (pink dots), and gene count (black bars on the outer side) per species for OG 98.

Figure S153. Species tree showing the origin (orange dot), losses (pink dots), and gene count (black bars on the outer side) per species for OG 114.

Figure S154. Species tree showing the origin (orange dot), losses (pink dots), and gene count (black bars on the outer side) per species for OG 124.

Figure S155. Species tree showing the origin (orange dot), losses (pink dots), and gene count (black bars on the outer side) per species for OG 153.

Figure S156. Species tree showing the origin (orange dot), losses (pink dots), and gene count (black bars on the outer side) per species for OG 154.

Figure S157 Species tree showing the origin (orange dot), losses (pink dots), and gene count (black bars on the outer side) per species for OG 155.

Figure S158. Species tree showing the origin (orange dot), losses (pink dots), and gene count (black bars on the outer side) per species for OG 175.

Figure S159. Species tree showing the origin (orange dot), losses (pink dots), and gene count (black bars on the outer side) per species for OG 193.

Figure S160. Species tree showing the origin (orange dot), losses (pink dots), and gene count (black bars on the outer side) per species for OG 195.

Figure S161. Species tree showing the origin (orange dot), losses (pink dots), and gene count (black bars on the outer side) per species for OG 228.

Figure S162. Species tree showing the origin (orange dot), losses (pink dots), and gene count (black bars on the outer side) per species for OG 255.

Figure S163. Species tree showing the origin (orange dot), losses (pink dots), and gene count (black bars on the outer side) per species for OG 257.

Figure S164. Species tree showing the origin (orange dot), losses (pink dots), and gene count (black bars on the outer side) per species for OG 295.

Figure S165. Species tree showing the origin (orange dot), losses (pink dots), and gene count (black bars on the outer side) per species for OG 342.

Figure S166. Species tree showing the origin (orange dot), losses (pink dots), and gene count (black bars on the outer side) per species for OG 436.

Figure S167. Species tree showing the origin (orange dot), losses (pink dots), and gene count (black bars on the outer side) per species for OG 459.

Figure S168. Species tree showing the origin (orange dot), losses (pink dots), and gene count (black bars on the outer side) per species for OG 487.

Figure S169. Species tree showing the origin (orange dot), losses (pink dots), and gene count (black bars on the outer side) per species for OG 492.

Figure S170. Species tree showing the origin (orange dot), losses (pink dots), and gene count (black bars on the outer side) per species for OG 498.

Figure S171. Species tree showing the origin (orange dot), losses (pink dots), and gene count (black bars on the outer side) per species for OG 706.

Figure S172. Species tree showing the origin (orange dot), losses (pink dots), and gene count (black bars on the outer side) per species for OG 707.

Figure S173. Species tree showing the origin (orange dot), losses (pink dots), and gene count (black bars on the outer side) per species for OG 737.

Figure S174. Species tree showing the origin (orange dot), losses (pink dots), and gene count (black bars on the outer side) per species for OG 864.

Figure S175. Species tree showing the origin (orange dot), losses (pink dots), and gene count (black bars on the outer side) per species for OG 896.

Figure S176. Species tree showing the origin (orange dot), losses (pink dots), and gene count (black bars on the outer side) per species for OG 902.

Figure S177. Species tree showing the origin (orange dot), losses (pink dots), and gene count (black bars on the outer side) per species for OG 912.

Figure S178. Species tree showing the origin (orange dot), losses (pink dots), and gene count (black bars on the outer side) per species for OG 943.

Figure S179. Species tree showing the origin (orange dot), losses (pink dots), and gene count (black bars on the outer side) per species for OG 977.

Figure S180. Species tree showing the origin (orange dot), losses (pink dots), and gene count (black bars on the outer side) per species for OG 1022.

Figure S181. Species tree showing the origin (orange dot), losses (pink dots), and gene count (black bars on the outer side) per species for OG 1202.

Figure S182. Species tree showing the origin (orange dot), losses (pink dots), and gene count (black bars on the outer side) per species for OG 1243.

Figure S183. Species tree showing the origin (orange dot), losses (pink dots), and gene count (black bars on the outer side) per species for OG 1484.

Figure S184. Species tree showing the origin (orange dot), losses (pink dots), and gene count (black bars on the outer side) per species for OG 1589.

Figure S185. Species tree showing the origin (orange dot), losses (pink dots), and gene count (black bars on the outer side) per species for OG 1647.

Figure S186. Species tree showing the origin (orange dot), losses (pink dots), and gene count (black bars on the outer side) per species for OG 1761.

Figure S187. Species tree showing the origin (orange dot), losses (pink dots), and gene count (black bars on the outer side) per species for OG 1810.

Figure S188. Species tree showing the origin (orange dot), losses (pink dots), and gene count (black bars on the outer side) per species for OG 2014.

Figure S189. Species tree showing the origin (orange dot), losses (pink dots), and gene count (black bars on the outer side) per species for OG 2088.

Figure S190. Species tree showing the origin (orange dot), losses (pink dots), and gene count (black bars on the outer side) per species for OG 2153.

Figure S191. Species tree showing the origin (orange dot), losses (pink dots), and gene count (black bars on the outer side) per species for OG 2188.

Figure S192. Species tree showing the origin (orange dot), losses (pink dots), and gene count (black bars on the outer side) per species for OG 2529.

Figure S193. Species tree showing the origin (orange dot), losses (pink dots), and gene count (black bars on the outer side) per species for OG 2725.

Figure S194. Species tree showing the origin (orange dot), losses (pink dots), and gene count (black bars on the outer side) per species for OG 2729.

Figure S195. Species tree showing the origin (orange dot), losses (pink dots), and gene count (black bars on the outer side) per species for OG 2783.

Figure S196. Species tree showing the origin (orange dot), losses (pink dots), and gene count (black bars on the outer side) per species for OG 2977.

Figure S197. Species tree showing the origin (orange dot), losses (pink dots), and gene count (black bars on the outer side) per species for OG 3068.

Figure S198. Species tree showing the origin (orange dot), losses (pink dots), and gene count (black bars on the outer side) per species for OG 3070.

Figure S199. Species tree showing the origin (orange dot), losses (pink dots), and gene count (black bars on the outer side) per species for OG 3192.

Figure S200. Species tree showing the origin (orange dot), losses (pink dots), and gene count (black bars on the outer side) per species for OG 3227.

Figure S201. Species tree showing the origin (orange dot), losses (pink dots), and gene count (black bars on the outer side) per species for OG 3244.

Figure S202. Species tree showing the origin (orange dot), losses (pink dots), and gene count (black bars on the outer side) per species for OG 3340.

Figure S203. Species tree showing the origin (orange dot), losses (pink dots), and gene count (black bars on the outer side) per species for OG 3377.

Figure S204. Species tree showing the origin (orange dot), losses (pink dots), and gene count (black bars on the outer side) per species for OG 3725.

Figure S205. Species tree showing the origin (orange dot), losses (pink dots), and gene count (black bars on the outer side) per species for OG 4119.

Figure S206. Species tree showing the origin (orange dot), losses (pink dots), and gene count (black bars on the outer side) per species for OG 4721.

Figure S207. Species tree showing the origin (orange dot), losses (pink dots), and gene count (black bars on the outer side) per species for OG 4723.

Figure S208. Species tree showing the origin (orange dot), losses (pink dots), and gene count (black bars on the outer side) per species for OG 4797.

Figure S209. Species tree showing the origin (orange dot), losses (pink dots), and gene count (black bars on the outer side) per species for OG 4937.

Figure S210. Species tree showing the origin (orange dot), losses (pink dots), and gene count (black bars on the outer side) per species for OG 5092.

Figure S211. Species tree showing the origin (orange dot), losses (pink dots), and gene count (black bars on the outer side) per species for OG 5724.

Figure S212. Species tree showing the origin (orange dot), losses (pink dots), and gene count (black bars on the outer side) per species for OG 5743.

Figure S213. Species tree showing the origin (orange dot), losses (pink dots), and gene count (black bars on the outer side) per species for OG 5822.

Figure S214. Species tree showing the origin (orange dot), losses (pink dots), and gene count (black bars on the outer side) per species for OG 5845.

Figure S215. Species tree showing the origin (orange dot), losses (pink dots), and gene count (black bars on the outer side) per species for OG 5881.

Figure S216. Species tree showing the origin (orange dot), losses (pink dots), and gene count (black bars on the outer side) per species for OG 6057.

Figure S217. Species tree showing the origin (orange dot), losses (pink dots), and gene count (black bars on the outer side) per species for OG 6081.

Figure S218. Species tree showing the origin (orange dot), losses (pink dots), and gene count (black bars on the outer side) per species for OG 6281.

Figure S219. Species tree showing the origin (orange dot), losses (pink dots), and gene count (black bars on the outer side) per species for OG 6359.

Figure S220. Species tree showing the origin (orange dot), losses (pink dots), and gene count (black bars on the outer side) per species for OG 6457.

Figure S221. Species tree showing the origin (orange dot), losses (pink dots), and gene count (black bars on the outer side) per species for OG 6604.

Figure S222. Species tree showing the origin (orange dot), losses (pink dots), and gene count (black bars on the outer side) per species for OG 6637.

Figure S223. Species tree showing the origin (orange dot), losses (pink dots), and gene count (black bars on the outer side) per species for OG 6693.

Figure S224. Species tree showing the origin (orange dot), losses (pink dots), and gene count (black bars on the outer side) per species for OG 6845.

Figure S225. Species tree showing the origin (orange dot), losses (pink dots), and gene count (black bars on the outer side) per species for OG 6905.

Figure S226. Species tree showing the origin (orange dot), losses (pink dots), and gene count (black bars on the outer side) per species for OG 7048.

Figure S227. Species tree showing the origin (orange dot), losses (pink dots), and gene count (black bars on the outer side) per species for OG 7348.

Figure S228. Species tree showing the origin (orange dot), losses (pink dots), and gene count (black bars on the outer side) per species for OG 7361.

Figure S229. Species tree showing the origin (orange dot), losses (pink dots), and gene count (black bars on the outer side) per species for OG 7407.

Figure S230. Species tree showing the origin (orange dot), losses (pink dots), and gene count (black bars on the outer side) per species for OG 7504.

Figure S231. Species tree showing the origin (orange dot), losses (pink dots), and gene count (black bars on the outer side) per species for OG 7509.

Figure S232. Species tree showing the origin (orange dot), losses (pink dots), and gene count (black bars on the outer side) per species for OG 7533.

Figure S233. Species tree showing the origin (orange dot), losses (pink dots), and gene count (black bars on the outer side) per species for OG 7534.

Figure S234. Species tree showing the origin (orange dot), losses (pink dots), and gene count (black bars on the outer side) per species for OG 7566.

Figure S235. Species tree showing the origin (orange dot), losses (pink dots), and gene count (black bars on the outer side) per species for OG 7796.

Figure S236. Species tree showing the origin (orange dot), losses (pink dots), and gene count (black bars on the outer side) per species for OG 8030.

Figure S237. Species tree showing the origin (orange dot), losses (pink dots), and gene count (black bars on the outer side) per species for OG 8323.

Figure S238. Species tree showing the origin (orange dot), losses (pink dots), and gene count (black bars on the outer side) per species for OG 8389.

Figure S239. Species tree showing the origin (orange dot), losses (pink dots), and gene count (black bars on the outer side) per species for OG 8407.

Figure S240. Species tree showing the origin (orange dot), losses (pink dots), and gene count (black bars on the outer side) per species for OG 8721.

Figure S241. Species tree showing the origin (orange dot), losses (pink dots), and gene count (black bars on the outer side) per species for OG 8831.

Figure S242. Species tree showing the origin (orange dot), losses (pink dots), and gene count (black bars on the outer side) per species for OG 8943.

Figure S243. Species tree showing the origin (orange dot), losses (pink dots), and gene count (black bars on the outer side) per species for OG 8985.

Figure S244. Species tree showing the origin (orange dot), losses (pink dots), and gene count (black bars on the outer side) per species for OG 9574.

Figure S245. Species tree showing the origin (orange dot), losses (pink dots), and gene count (black bars on the outer side) per species for OG 9700.

Figure S246. Species tree showing the origin (orange dot), losses (pink dots), and gene count (black bars on the outer side) per species for OG 9701.

Figure S247. Species tree showing the origin (orange dot), losses (pink dots), and gene count (black bars on the outer side) per species for OG 9705.

Figure S248. Species tree showing the origin (orange dot), losses (pink dots), and gene count (black bars on the outer side) per species for OG 9719.

Figure S249. Species tree showing the origin (orange dot), losses (pink dots), and gene count (black bars on the outer side) per species for OG 9991.

Figure S250. Species tree showing the origin (orange dot), losses (pink dots), and gene count (black bars on the outer side) per species for OG 10041.

Figure S251. Species tree showing the origin (orange dot), losses (pink dots), and gene count (black bars on the outer side) per species for OG 10090.

Figure S252. Species tree showing the origin (orange dot), losses (pink dots), and gene count (black bars on the outer side) per species for OG 10205.

Figure S253. Species tree showing the origin (orange dot), losses (pink dots), and gene count (black bars on the outer side) per species for OG 10298.

Figure S254. Species tree showing the origin (orange dot), losses (pink dots), and gene count (black bars on the outer side) per species for OG 10407.

Figure S255. Species tree showing the origin (orange dot), losses (pink dots), and gene count (black bars on the outer side) per species for OG 10427.

Figure S256. Species tree showing the origin (orange dot), losses (pink dots), and gene count (black bars on the outer side) per species for OG 10479.

Figure S257. Species tree showing the origin (orange dot), losses (pink dots), and gene count (black bars on the outer side) per species for OG 10510.

Figure S258. Species tree showing the origin (orange dot), losses (pink dots), and gene count (black bars on the outer side) per species for OG 10512.

Figure S259. Species tree showing the origin (orange dot), losses (pink dots), and gene count (black bars on the outer side) per species for OG 10656.

Figure S260. Species tree showing the origin (orange dot), losses (pink dots), and gene count (black bars on the outer side) per species for OG 10708.

Figure S261. Species tree showing the origin (orange dot), losses (pink dots), and gene count (black bars on the outer side) per species for OG 10713.

Figure S262. Species tree showing the origin (orange dot), losses (pink dots), and gene count (black bars on the outer side) per species for OG 10762.

Figure S263. Species tree showing the origin (orange dot), losses (pink dots), and gene count (black bars on the outer side) per species for OG 10970.

Figure S264. Species tree showing the origin (orange dot), losses (pink dots), and gene count (black bars on the outer side) per species for OG 11043.

Figure S265. Species tree showing the origin (orange dot), losses (pink dots), and gene count (black bars on the outer side) per species for OG 11183.

Figure S266. Species tree showing the origin (orange dot), losses (pink dots), and gene count (black bars on the outer side) per species for OG 11206.

Figure S267. Species tree showing the origin (orange dot), losses (pink dots), and gene count (black bars on the outer side) per species for OG 11214.

Figure S268. Species tree showing the origin (orange dot), losses (pink dots), and gene count (black bars on the outer side) per species for OG 11303.

Figure S269. Species tree showing the origin (orange dot), losses (pink dots), and gene count (black bars on the outer side) per species for OG 11582.

Figure S270. Full functions from the top 10 OGs as ranked by the machine learning model. The OG names were obtained with BLASTp. GO terms on the right were predicted using FANTASIA.

Figure S271. MPR ancestral habitat reconstruction (aquatic in blue, terrestrial in brown). Red branches represent ambiguous reconstruction.

Figure S272. Manually modified MPR ancestral habitat reconstruction based on known information from previous studies. Aquatic branches are in blue, terrestrial in brown.

Figure S273. PCA and heatmap of *C. elegans* RNA-seq samples using normalized counts (top) and after batch effect correction (bottom).

Figure S274. PCA and heatmap of *L. marina* RNA-seq samples using normalized counts (top) and after batch effect correction (bottom).

Figure S275. PCA and heatmap of *P. aurorbis* RNA-seq samples using normalized counts (top) and after batch effect correction (bottom).

Figure S276. PCA and heatmap of *P. laevis* RNA-seq samples using normalized counts (top) and after batch effect correction (bottom).

Figure S277. PCA and heatmap of *L. oceanica* RNA-seq samples using normalized counts (top) and after batch effect correction (bottom).

Figure S278. PCA and heatmap of *O. nungara* RNA-seq samples using normalized counts (top) and after batch effect correction (bottom).

Figure S279. PCA and heatmap of *S. mediterranea* RNA-seq samples using normalized counts (top) and after batch effect correction (bottom).

Figure S280. PCA and heatmap of *P. turbinatus* RNA-seq samples using normalized counts (top) and after batch effect correction (bottom).

Figure S281. PCA and heatmap of *S. pectinata* RNA-seq samples using normalized counts (top) and after batch effect correction (bottom).

Figure S282. PCA and heatmap of *T. pisana* RNA-seq samples using normalized counts (top) and after batch effect correction (bottom).

Figure S283. PCA and heatmap of *P. acuta* RNA-seq samples using normalized counts (top) and after batch effect correction (bottom).

Figure S284. PCA and heatmap of *A. marina* RNA-seq samples using normalized counts (top) and after batch effect correction (bottom).

Figure S285. PCA and heatmap of *E. andrei* RNA-seq samples using normalized counts (top) and after batch effect correction (bottom).

Figure S286. PCA and heatmap of *H. medicinalis* RNA-seq samples using normalized counts (top) and after batch effect correction (bottom).

Figure S287. PCA and heatmap of *L. chalicophora* RNA-seq samples using normalized counts (top) and after batch effect correction (bottom).

Figure S288. PCA and heatmap of *T. melanocephalum* RNA-seq samples using normalized counts (top) and after batch effect correction (bottom).

Figure S289. PCA and heatmap of *T. longissimum* RNA-seq samples using normalized counts (top) and after batch effect correction (bottom).

Figure S290. Machine learning data stratification, workflow, and results. a, Data splitting into 5 stratified folds based on habitat and phylogenetic categories. **b**, Proportion of each phylogenetic category ("phylum") in the testing and training datasets for each of the 5 folds. **c**, Proportion of each habitat in the testing and training datasets for each of the 5 folds. **d**, Dynamic recursive feature elimination (dRFE) workflow.